Neutron Star Kinetic Heating through Dark Matter Subhalo Encounters

Benjamin Mendez

A Thesis Submitted to the Faculty of Graduate Studies
in Partial Fulfillment of the Requirements
for the Degree of

Master of Science

Graduate Program in Physics & Astronomy
York University
Toronto, Ontario

June, 2026
©Benjamin Mendez, 2026

Abstract

Celestial bodies, such as stars or exoplanets, can capture dark matter (DM) particles if they scatter with atomic nuclei and deposit their kinetic energy. This kinetic heating process can raise the temperature of the bodies above expectations. Old, cold neutron stars are an ideal probe of DM due to their high densities and low temperatures. We present a stochastic simulation of an old neutron star encountering multiple DM clumps called subhalos. We calculate the temperature evolution during and between halo encounters for a wide range of subhalo masses and radii. Our simulations show a significant increase in the mean temperature over the star's encounter history in the DM substructure paradigm. We use these results to estimate the IR flux from old neutron stars to show future observations with IR telescopes can be used for testing small-scale DM distributions and DM interactions with visible matter.

Contents

Page

Abstract ii

Contents iii

List of Figures v

1 Introduction 1

1.1 A Brief History of Dark Matter . . . 2

2 Dark Matter Particle Model 8

2.1 Direct Detection (DD) and the Neutrino Floor . . . 8

2.2 Indirect Detection (ID) of Dark Matter . . . 10

2.3 Asymmetric Dark Matter . . . 11

3 Dark Matter Capture in Celestial Bodies 13

3.1 Relevant Bodies for Study . . . 13

3.2 Physical Interactions Leading to Capture . . . 15

3.3 General Formalism for Capture . . . 16

4 Dark Matter Capture from Clumpy Distributions 19

4.1 Cosmology of Dark Matter Substructure . . . 19

4.2 Subhalo Profiles . . . 21

4.3 Subhalo Encounters . . . 22

4.4 Clumpiness of Distribution . . . 24

5 Neutron Stars as Dark Matter Laboratories 27

5.1 Neutron Star Formation and Structure . . . 27

5.2 Previous Studies of Neutron Star Kinetic Heating . . . 28

5.3 Neutron Star Thermalization . . . 28

5.4 Neutron Star Cooling . . . 29

5.4.1 Time Spent at Elevated Temperature . . . 35

6 Numerical Solutions to Neutron Star Cooling Curves 36

6.1 Cooling Inside and Outside of Halos . . . 37

6.2 Generating an Encounter History . . . 37

6.3 Subhalo Parameter Space . . . 38

6.4 Numerically Solving Neutron Star Cooling Curves . . . 39

7 Results 41

7.1 Temperature Results . . . 41

7.2 Time Spent Above 1000 K, f_{elev} . . . 43

7.3 Observation Prospects . . . 45

8 Conclusion 50

Bibliography 52

Appendices 56

A Dark Matter Energy Depletion . . . 56

B Parameter Sampling Distributions . . . 60

B.1 Time Between Encounters τ_{enc} . . . 60

B.2 Impact Parameter b_{Imp} . . . 61

C Neutron Star Cooling Curves - Example Derivations . . . 62

C.1 Cooling Curve from Photon Emission . . . 62

C.2 Cooling Curve for a Uniform Density Halo . . . 63

C.3 Cooling Curve for DM Halo with a Parabolic Density Profile . . . 64

List of Figures

1 Galactic and solar systems rotation curves . . . 3

2 Bullet Cluster X-Ray and Optical image from Chandra X-Ray Observatory . . . 5

3 CMB Planck power spectrum . . . 6

4 Dark matter particle mass candidates . . . 8

5 Experimental constraints of WIMP-nucleon scattering cross section . . . 9

6 Constrains on DM annihilation cross sections from ID experiments . . . 10

7 Feynman diagrams of DM scattering and annihilation interactions . . . 12

8 DM-nucleon scattering cross section constraints for various celestial bodies . . . 14

9 DM-nucleon scattering diagram in center of mass frame . . . 15

10 Core vs. cusp dark matter density profiles . . . 19

11 Small scale power spectrum perturbations due to modifications of inflation . . . 21

12 Geometric illustration of neutron star encounter with a dark matter subhalo; Plot of dark matter subhalo NFW density profile cross sections . . . 23

13 Encounter rate contour plot of the dark matter subhalo parameter space (M_h, R_h) with smoothness parameter s constraint . . . 25

14 Neutron star cooling curve during neutrino emission cooling phase . . . 29

15 Example neutron star cooling curve during an encounter with an NFW subhalo . . . 34

16 Numerical & analytic solutions for neutron star cooling curves; photon emission and parabolic halo densities . . . 36

17 Neutron star encounter history and cooling curve; zoomed in plot of a single encounter with a uniform density subhalo . . . 39

18 Contour plots of the mean temperature $\bar{T}_w$ and fraction of time spent at an elevated temperature f_{elev} for NFW and uniform suhalo densities . . . 42

19 Mean temperature histograms NFW and uniform density subhalos . . . 44

20 Cooling curve figures showing approach to steady state . . . 46

21 Parameter space contour plots of spectral flux densities . . . 47

22 DM-neutron scattering cross section constraints for given theorized neutron star observations 48

23 Sampling distribution plots for time between encounters τ_{enc} and impact parameter b_{Imp} . . . 60

1 Introduction

The nature of dark matter (DM) has been a primary yet elusive component in cosmology since it was initially theorized by Fritz Zwicky in 1933 [1]. Observations appear to point toward a cold DM (CDM) theory that has no coupling to the Standard Model (SM), only interacting with baryonic matter gravitationally. The Standard Model of particle physics describes all the particles currently discovered and how they interact with each other. It has become one of the most successful theories in modern physics, providing accurate predictions of experiments and aiding in crucial discoveries across energy regimes.

N-body simulations of CDM, which focus on large-scale structure formation, reinforce this theory when compared to cosmological probes such as the Cosmic Microwave Background (CMB) [2]. To align with CMB observations, ΛCDM cosmology prescribes an energy budget for the Universe. This considers 3 primary components, $\sim 0.0084\%$ radiation (photons + neutrinos), 30% matter (visible matter + dark matter), and 70% dark energy. DM contributes 26% to the Universe, leaving visible matter at a meager 4%. Issues begin to arise when we look at small-scale structure, such as galactic halos and their density profiles, determined by circular velocity measurements. This problem is a discrepancy between inner region DM halos from observed galaxies and those predicted by CDM simulations [3]. This is known as the "core-cusp" problem [4], referring to the "cuspy" profile resulting from CDM compared to the cored profiles seen by observations. This has called into question the validity of CDM on small-scales, specifically how DM behaves and is distributed on subgalactic scales. This has opened the door for various theoretical models on the nature of DM on a particle level that could remedy small-scale structure problems while remaining consistent with large-scale CDM observations.

There are many methods that are being used in an attempt to identify the nature of DM. If there is a coupling between the dark sector and SM, then this means that a DM particle could interact with SM particles and/or nuclei. Earth-based detectors employ direct and indirect detection methods to probe into this potential coupling; direct detectors focus on DM particle scattering with atomic nuclei, indirect detectors seek to observe decay or annihilation products. We dive into the basic principles of these experiments in Section 2.1. Despite the increase in detector sensitivities over the years, no confirmed DM scattering events or decay/annihilation products have been observed. This has aided in imposing strong constraints on DM models, particularly in the $\mathrm{GeV} - \mathrm{PeV}$ mass range. With these constraints, the question regarding the particle nature of DM lives on.

Although beneficial in guiding the minds of theorists, many of the intermediate mass models for CDM have been ruled out due to these direct detection experiments. To allow for continued exploration of these models, this thesis studies the DM halo distribution of the Milky Way, comparing the standard smooth profile with a clumpy distribution composed of many DM subhalos. Using this, we can bypass current direct detection bounds, providing freedom to explore various models with larger DM-SM interaction cross-sections. We outlined the use of neutron stars as DM capture targets to study kinetic heating effects due to DM-neutron scattering. This thesis is organized as follows. In Sections 1.1 and 2 we review the history of DM and the key discoveries that have motivated leading models. In Section 3 we explore the concept of DM capture in celestial bodies and which objects are ideal candidates for study. In Section 4 we outline the clumpy and smooth paradigms for the density distribution of galactic DM halos. In Section 5 we focus on neutron stars as DM probes and how we utilize their cooling evolution as a probe for dark kinetic heating. In Section 6 we detail our multi-encounter simulation for calculating the cooling curves of our benchmark neutron star. In Sections 7 and 8 we lay out the results of our simulation, its implications, and next steps for building on this thesis.

1.1 A Brief History of Dark Matter

Since Fritz Zwicky first hypothesized dark matter (DM) in 1933 [1] there have been many attempts to unravel the true nature of this exotic component of the cosmos. A significant fraction of matter in the Universe, $\sim 26\%$ [5], is composed of DM. This is in large contrast to baryonic matter which comprises $\sim 5\%$ of matter. Zwicky utilized the virial theorem to show the observed velocity dispersion of the Coma Cluster required a large amount of extra matter in order to explain the high velocities. Visible (baryonic) matter from the constituent galaxies was shown to be a subdominant component in the Coma Cluster and further work in the 1970s by Vera Ruben in her observations of flattened galactic rotation curves (left plot in Figure 1) provided further evidence to the existence of DM [6]. The presence of DM was a groundbreaking discovery, but the nature of what DM really is continues to be an area of important study.

In this Section we will review key pieces of evidence for DM consisting of the following observations and discoveries; galactic rotation curves, the Bullet Cluster matter density distribution, the Coma Cluster and its peculiar velocities, and the CMB power spectrum evidence for DM on large-scales.

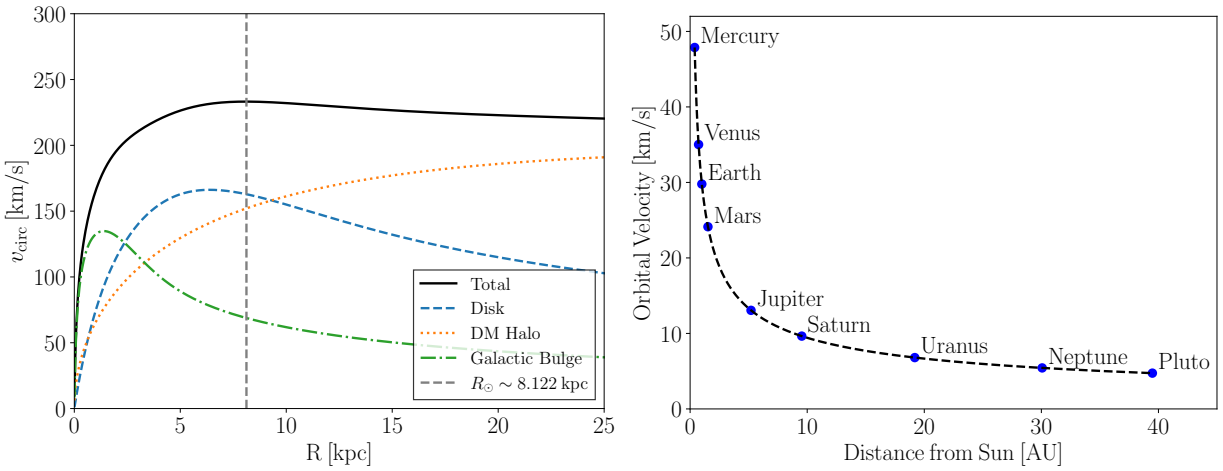

Figure 1: **Left:** Rotation curve of the Milky Way with all components separated. We see that visible matter (disk + bulge) impact the rotation curve in the inner region of the galaxy, while the outer region is dominated by the DM halo. The gray dashed line signifies the position of the Sun in the Milky Way. **Right:** Rotation curve of planets in the Solar System, showing how Newtonian motion tends to result in decreasing velocity as you get further from the mass distribution, i.e., the Sun.

Rotation Curves

Another defining discovery in history of DM is invaluable work done by Vera Rubin on galaxy rotation curves. When considering the rotational velocity of objects such as stars and gas within a system like a galaxy, the expectation is that the rotational velocity would increase, peak, and start to decline as you get farther from the center of the system. This is the Newtonian motion we are familiar with in our Solar system, as seen in right-hand of Figure 1. What Rubin saw in her analysis of multiple rotation curves of various galaxies with varying luminosities and radii [7] is that regardless of their size and radius, the rotational velocities continue to rise or flatten at larger radii, seen in the left-hand of Figure 1. This implied a "missing" mass that prevents the velocity from dropping in the outer regions of galaxies - galactic DM halos. These halos are composed of DM, hosting a galaxy and extending far past its visible outer regions. The distributions of these halos have been inferred by studying the motions of stars and gas, fitting the density profile to match the rotation curves of the host galaxy.

The presence of DM halos hosting galaxies was an important discovery that continues to be an important area of study. Halos have opened research into the structure of DM, its formation, and evolution in cosmology. They have also opened questions regarding the nature of DM, specifically its particle nature and if it truly only interacts with baryonic matter through gravity.

The Bullet Cluster

In 2003, Clowe, Gonzalez, and Markevitch [8] studied optical and X-ray observations of the Bullet Cluster, from the Chandra X-ray Observatory shown in Figure 2. In their work they consider a weak lensing reconstruction that aimed to differentiate the components of the cluster. The cluster was discovered in early 1990s and is a pair gas clouds that have collided with each other. X-ray emission is observed in the central regions of the collisions, with an impact shock visible through the middle of the interaction. The work performed in [8] showed gravitational lensing effects on the outer regions of the interaction. This is seen as distorted light from objects behind the cluster, such as galaxies, bending around the high density regions. These high density regions do not align with the X-ray emission from the central region, which is where the visible gas is concentrated. These are seen as the red (X-ray emission) and purple (lensing) filters in Figure 2. This raises the question of what is causing the lensing in regions where visible matter is absent. Theories of modified gravity, e.g., Modified Newtonian Dynamics (MOND), are not able to fully explain this offset in gravitational potential that is observed, signaling further evidence to the theory that DM is present in the cluster and is potentially collisionless due to the positioning of the lensing effects. Weakly interacting DM is the leading candidate due to the distributions that cause the lensing appear to imply they had passed through each other. This has helped constrain DM models with self-interactions since DM-DM interactions (e.g., scattering) would result in a larger distribution in the central region of the cluster.

The Coma Cluster

The first mention of the existence of DM comes from Fritz Zwicky in his work from 1933 on the velocity dispersion of galaxies in the Coma Cluster. His work considered the mass of the cluster determined by the virial theorem and compared it to its luminosity using the Mass-Luminosity relation [10]. The luminosity of the coma cluster has been determined to be $L_{\text{Coma}} \sim 2 \times 10^{13}\, L_{\odot}$ [11]. Assuming the system is isolated, the virial theorem provides a relation between the kinetic (K) and potential (U) energy of the ensemble through the second time derivative of the moment of inertia I of the cluster,

$$\ddot{I} = 2U + 4K \tag{1.1}$$

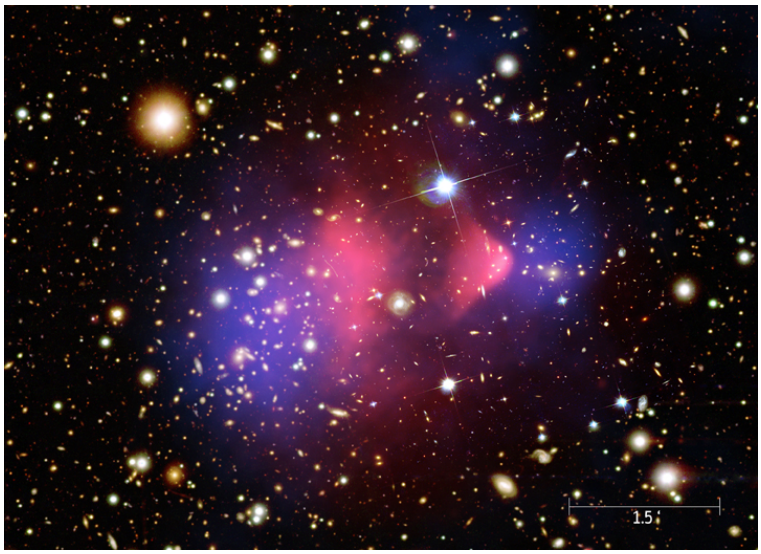

Figure 2: X-Ray (red filter) and optical lensing (purple filter) image of gas in the Bullet Cluster taken by the Chandra X-Ray Observatory [9]. Lensing shows that there are overdensities at the outer regions of the cluster that can be explained as being the DM from each cluster that passed through impact. X-Ray imaging shows the distribution of visible matter lies in the central region, away from the overdensities observed by lensing.

where K and U are the kinetic and gravitational potential energy of the cluster. If we also assume the system is in a steady state, then $\ddot{I} = 0$ which gives,

$$K = -\frac{U}{2}$$

For Coma, consider the system to be made up of galaxies with mean square velocity $\langle v^2 \rangle$, which gives the kinetic energy of the system,

$$K = \frac{1}{2} M \langle v^2 \rangle \tag{1.2}$$

The gravitational potential energy can be determined by considering how much energy is required to pull each particle (galaxy) away from each other particle to infinity;

$$U = -\frac{G}{2} \sum_{\substack{i,j \\ j \neq i}} \frac{m_i m_j}{|\mathbf{x}_j - \mathbf{x}_i|}$$

We can take each galaxy to be a test particle, with the other galaxies treated as a spherical lump of mass $M = \sum m_i$. Under this assumption, the potential energy of the cluster can then be written as,

$$U = \frac{3GM^2}{5R_{\mathrm{HM}}} \tag{1.3}$$

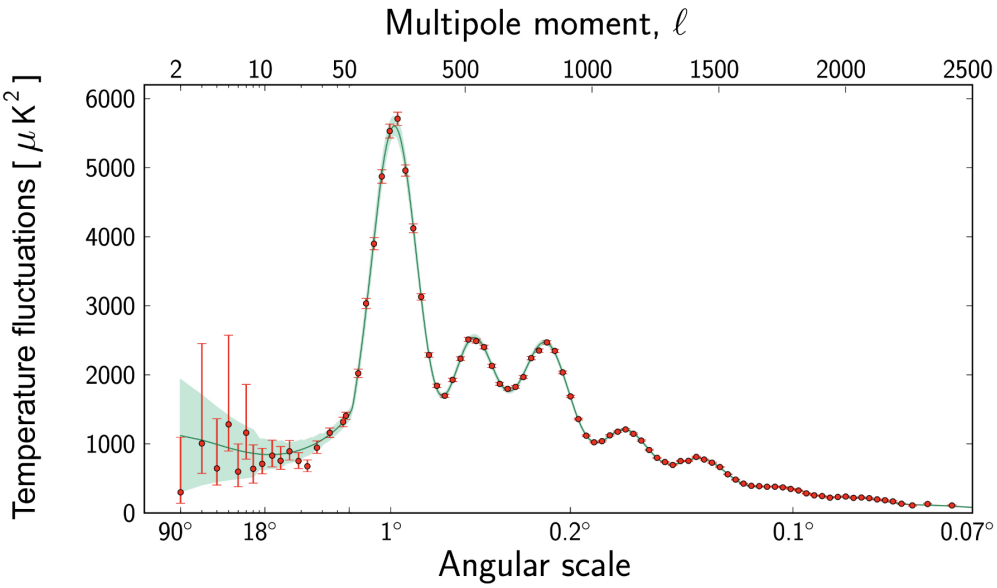

Figure 3: CMB power spectrum from the Planck observatory (red dots) with the standard cosmology ΛCDM fit (green curve). The y-axis represents the squared temperature fluctuations of CMB photons at various angular scales θ/multipole moments l on the x-axes.

where $R_{\rm HM}$ is the half-mass radius within which half of the cluster mass is contained. Using the virial theorem in equation (1.1) the kinetic energy of the cluster in equation (1.2), and the potential energy in equation (1.3), the mass of the cluster is then,

$$M = \frac{5\langle v^2\rangle R_{\rm HM}}{3G} \tag{1.4}$$

The Coma Cluster being positioned at a redshift of $z = 0.0232$ gives a line-of-sight (l.o.s.) velocity dispersion of $\sigma = 880\,\mathrm{km/s} \rightarrow \sigma_{3D} = 3\sigma = 2460\,\mathrm{km/s}$. This results in a mean square velocity of $\langle v^2\rangle = 2.32 \times 10^{12}\,\mathrm{m^2 s^{-2}}$. With a half-mass radius of $R_{\rm HM} = 1.5\,\mathrm{Mpc}$, the mass of the Coma cluster using the virial theorem is $M_{\rm Coma} \approx 2 \times 10^{15}\,\mathrm{M}_\odot$. The mass-luminosity relation of the cluster is then $M_{\rm Coma}/L_{\rm Coma} \sim 100\,M_\odot/L_\odot$. Zwicky's results had determined a mass-luminosity of ~ 500, which although the calculation we show is substantially smaller, still shows the discrepancy that he had discovered in his initial findings. DM greatly dominates over luminous matter in the Coma cluster, and this discovery would not be the only example nor the only scale to which this asymmetry is found.

Cosmic Microwave Background

The Cosmic Microwave Background (CMB) was a pivotal discovery in cosmology. The photons we observe from the CMB are a snapshot of the last scattering surface, the moment when a CMB photon had last scattered with an electron. This shows the moment when the Universe went from opaque to transparent due to the expansion rate of the Universe being faster than the scattering rate of photons with electrons. From its initial discovery in 1964 by Robert Wilson and Arno Penzias [12], the CMB has provided some of the most concrete evidence for the history and evolution of the Universe, as well as its composition of matter, radiation, and dark energy. The observation of CMB radiation is also the strongest evidence we have of a hot Big Bang, with prior theories proposing the existence of background radiation if the Universe started in a hot dense state [13]. The power spectrum of the CMB (Figure 3) shows how well the ΛCDM cosmological model agrees with large scale structure formation and evolution. This model consists of a dark energy component, denoted by Λ, a radiation component, and a matter component comprised of visible/baryonic matter + DM. The first peak allowed us to determine the photon-to-baryon ratio due to the coupling between baryons and radiation, while DM has no such coupling and is essentially transparent to photons. This reveals that visible matter only contributes $\sim 4\%$ to the energy density. To have the ΛCDM model fit the observed power spectrum, there is a remaining 31% in matter that must be accounted for; yet more evidence supporting the existence of DM. This tells us that the fraction of DM in the Universe is significantly larger than visible matter, meaning the amount of DM is a key component in how the CMB currently looks.

The evidence of DM we have presented reveals how crucial a role it plays in our Universe, from early stages of cosmology to how it affects the motions of visible matter through gravity, yet we still have no concrete knowledge of its nature on a particle level. This has led to extensive studies, both theoretical and experimental, into developing models that can explain observations.

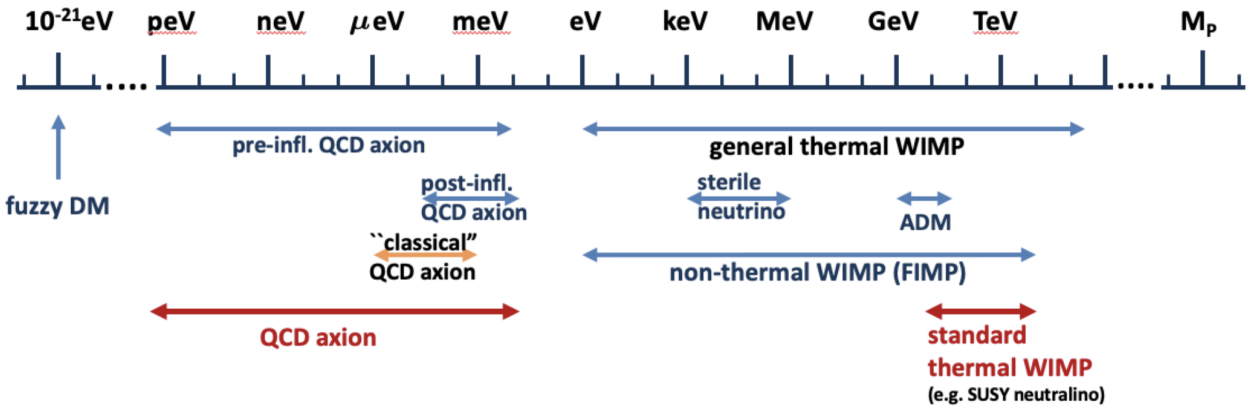

Figure 4: Mass range of DM particle candidates from Billard et al. [14]. The two leading theories of DM are axions and WIMPs. The axion is a very light theorized particle that arises from a solution to the strong CP problem in particle physics [15]. WIMPs are particles that are thought to interact very weakly with visible matter, but are massive enough explain the "missing" matter component in the Universe.

2 Dark Matter Particle Model

Many models have been developed to describe how DM interacts with the SM and/or itself. The gravitational interactions due to DM can be described by many particle models, ranging over many masses as seen in Figure 4. There are also theories that propose other methods of interaction, including scattering and/or annihilation/decay events. Direct detection (DD) and indirect detection (ID) experiments are used to probe nuclear recoils from scattering events with SM particles, or potential SM products of annihilation/decay. We note that for DD, the GeV – TeV mass range has been heavily studied. In this thesis, we consider a particle mass of $m_\chi = 100\,\text{GeV}$ that lies within DD considerations. A range of masses can be considered, resulting in slight adjustments in the energy deposited during capture ΔE (see Section 3.2).

In this Section we will give a brief overview of detection methods and techniques that are actively used to potentially probe DM couplings with the SM. We then go over the asymmetric/inelastic DM models and describe our motivation for using one such model for this thesis.

2.1 Direct Detection (DD) and the Neutrino Floor

Strong observational evidence has shown the existence of DM is crucial to the cosmology of our Universe. The persisting problem lies in understanding what DM actually is and how it interacts with baryonic matter past gravitational influences. If DM is a particle with some form of coupling with the Standard Model, then direct detection experiments should pick up signals of scattering events. Detectors such as XENONnT, focus

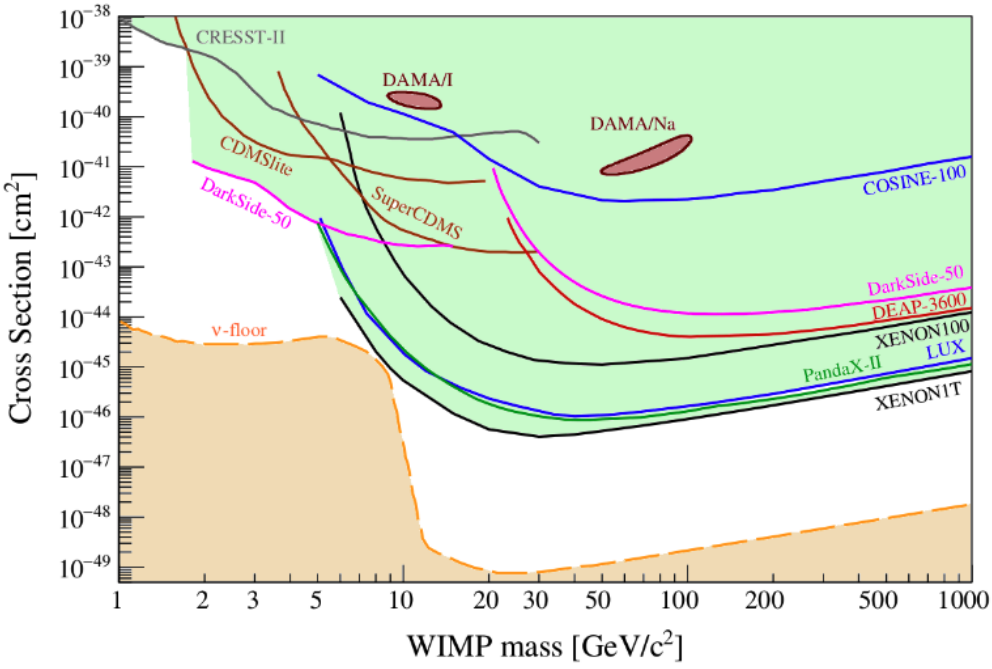

Figure 5: DM-nucleon interaction cross-section constraints from DD experiments (Lin 2019 [16]). The solid lines indicate the mass ranges considered by each experiment, above which all values for the DM-nucleon cross-sections are ruled out. The green region is a cumulative constraint from all Earth-based DD experiments. The orange region represents the neutrino-floor within which any detections made would be indistinguishable to background neutrino noise.

on trying to observe low-energy scattering events while minimizing detections of background interactions. For the example of the XENONnT detector, the principle of detection considers a WIMP particle scattering with the liquid xenon nuclei, resulting in a nuclear recoil from the ionization and excitation of the xenon target [17]. The two scintillator detectors, S1 and S2, focus on detecting photons emitted from the initial scattering event (S1) and electrons freed by ionization (S2). To distinguish between a DM and background interaction, the scintillation-to-ionization ratio of a given event is used. WIMPs are theorized to produce nuclear recoils during scattering (S1 detector), whereas the background primarily produces ionization (S2 detector) [18]. Figure 5 shows the upper limit constraints on the DM-nucleon cross-section for a range of DM particle masses. For the GeV-TeV mass range, we see the constraints have left promising regions to focus on with future experiments. We also see that shrinking parameter space is approaching what is known as the neutrino floor. This is a region within which potential DM-nuclei interactions would be indistinguishable to background neutrinos interacting with ground-based detectors due to their high sensitivities. If we do reach this point, this would require improved methods in distinguishing between these background neutrinos, or exploring other methods to probe smaller cross-sections. We also note that DM masses $m_\chi <$ GeV and

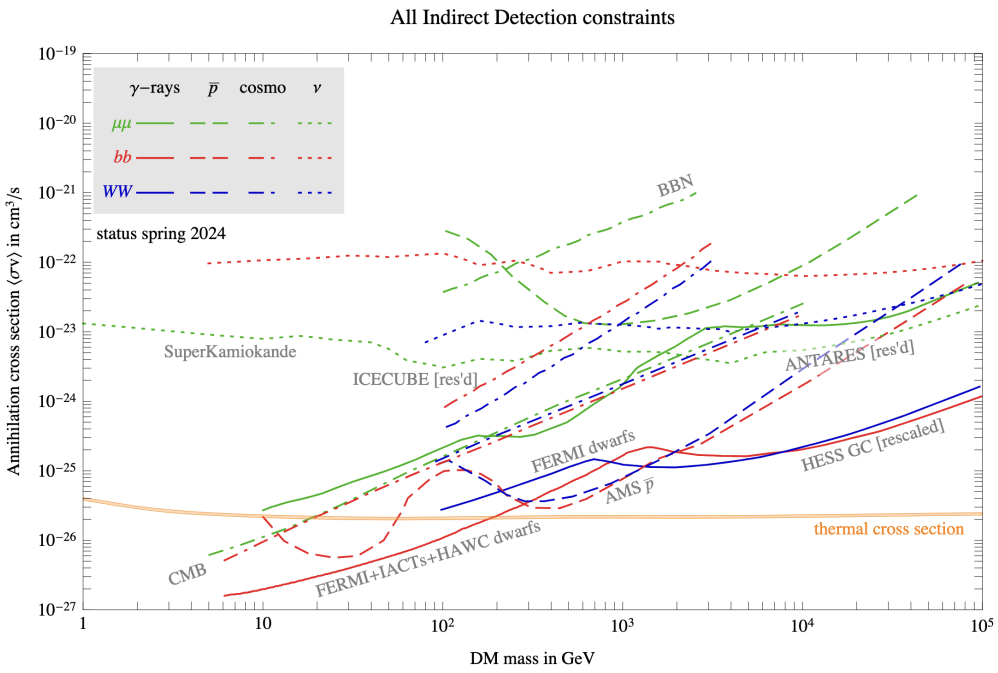

Figure 6: Thermally-averaged annihilation cross-section constraints from indirect detection observations for various DM masses (Cirelli 2024 [19]). Each experiment, denoted by the solid and dashed lines, show the mass ranges considered by each study and their corresponding upper limits to $\langle \sigma v_{\text{rel}} \rangle$. The orange band is the thermal cross-section based off the measured DM relic abundance.

$m_\chi >$ TeV are still largely unconstrained by DD experiments.

2.2 Indirect Detection (ID) of Dark Matter

Some DM models theorize a coupling to the SM through annihilation/decay events. When DM particles annihilate or decay, they can produce SM products such as photons and fermions (e.g., electrons, protons, neutrinos) [19]. In the case that DM self-interactions/decays result in photon production (e.g., gamma rays), some detection methods focus on observing regions of high DM density with minimal background. Examples include the galactic center of the Milky Way, subhalos in the galactic halo, and low-surface brightness galaxies.

ID studies have also probed into DM annihilation and decay channels from capture in celestial bodies such as stars [20]. When DM is captured, it can annihilate with a particle/anti-particle already present in the body. The mediator of this interaction can decay within the body, depositing energy (or produce neutrinos that could escape and be detected) that can result in heating. If the mediator decays outside the body, then it can produce SM particles that could also be detected.

One way ID probes dark matter is by studying the thermally averaged cross-section (annihilation) $\langle \sigma v_{\text{rel}} \rangle$.

$\langle \sigma v_{\text{rel}} \rangle$ encodes the rate of annihilation for DM, considering the relative velocity between particles in a thermal bath in the early Universe and the annihilation cross section. From this the relic abundance can be inferred. Standard cosmology sets the DM abundance in the Universe at $\sim 26\%$, implying a value for $\langle \sigma v_{\text{rel}} \rangle =$ on the order of $10^{-26}\,\text{cm}^2/\text{s}$. If a model for DM predicts an annihilation cross-section too large or too small, then it would result in relic abundances too high or too low compared to observations [19]. Based on this, ID searches would need to be consistent with the relic abundance. The difficulty in this method lies in the astrophysical factor (J-factor) [21] which is dependent on knowing the DM density distribution. Since the distributions of targets such as the galactic center, clusters, or galaxy halos are not known, this introduces uncertainties into the analysis observations. Despite this, ID methods have been successful in constraining DM mass ranges, as seen in Figure 6.

2.3 Asymmetric Dark Matter

We now introduce and motivate asymmetric DM as our model of choice for this thesis. There are particle theories of DM that consider couplings to the SM by annihilating and/or decaying into SM products. Indirect detection experiments are designed to detect the products of annihilation/decay, as outlined in Section 2.2. Additionally, there are models that have couplings to the SM through scattering interactions. These are studied through the direct detection experiments we described in Section 2.1. As mentioned, a drawback with ID is the reliance on knowing the DM density of the region being observed. This paired with the absence of DM annihilation/decay signals gives motivation to explore models that do not couple to the SM through such interactions. This thesis focuses on the effects of DM scattering with SM fermions (e.g., neutrons) as seen in Baryakhtar et al. [22]. We also note the absence of signals from DD experiments means we must consider a further modification to standard DM. This can be done by considering the DM galactic distribution to be composed of substructure. This allows us to remain consistent with DD constraints by assuming the Earth has not passed through a substructure since these experiments have begun. We dive deeper into this distribution of DM in Section 4.

To describe the model we use for our work, we consider an effective Lagrangian for the coupling between a fermionic DM particle χ, and fermionic SM particle, denoted as ξ (or neutrons n). This Effective Field Theory (EFT) is laid out in Joglekar et al. [23] using the O_1^F contact operator,

$$\mathcal{L}_{\chi\xi} = \frac{1}{\Lambda^2}\left(\bar{\chi}\chi\right)\left(\bar{\xi}\xi\right) \rightarrow \mathcal{L}_{\chi n} = \frac{1}{\Lambda^2}\left(\bar{\chi}\chi\right)\left(\bar{n}n\right) \tag{2.1}$$

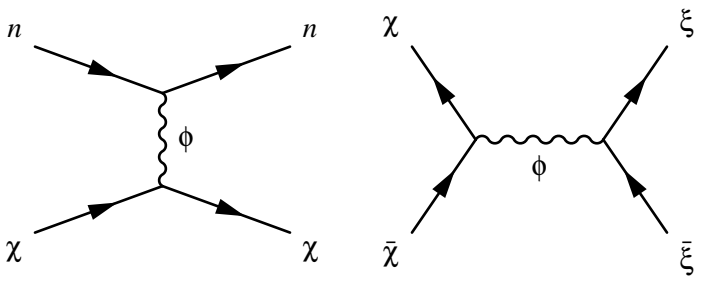

Figure 7: **Left:** Scattering interaction of a fermionic DM particle χ with a neutron n. **Right:** Annihilation of DM particle-antiparticle pair $\bar{\chi}\chi$ resulting in SM fermion products $\bar{\xi}\xi$. Both figures show the interactions mediated by a scalar boson ϕ.

where Λ is the cutoff scale that parameterizes the strength of DM-SM interactions. Figure 7 shows the scattering diagram DM interacting with a neutron, mediated by a scalar boson ϕ. The model shown in the EFT Lagrangian in equation (2.1) considers a heavy mediator. This is beneficial in simplifying the momentum transfer of the interaction, where the mass of the mediator dominates over the couplings. This gives us the cutoff scale to be proportional to the mediator mass [23]. We take the neutron star to be a neutron fluid, allowing us to solely consider kinetic heating from DM particles scattering with neutrons. In the contact operator from the EFT operator in equation (2.1), DM consists of particle-antiparticle pairs. Since our thesis focuses on scattering events as the cause of neutron star heating, any annihilation interactions must be extremely rare or nonexistent to yield negligible heating effects. There are two ways to allow this from a physical standpoint [16, 24];

- **DM is asymmetric in nature** - Anti-particle population is scarce compared to particle counterpart, leading to low annihilation rates.
- **Inelastic DM** - DM was initially two states; a lighter DM particle χ_- and a heavier particle χ_+. χ_- can scatter and excite to χ_+, which can be longer lived and be a significant fraction of the DM population

We have explored the ID and DD methods for DM experiments, providing our motivation for an asymmetric/inelastic particle model. We now move to discuss how DM can interact with the SM by scattering with particles in celestial bodies such as stars. This provides the basis of the simulations we have developed and will detail in Section 6.

3 Dark Matter Capture in Celestial Bodies

In this Section we outline DM capture in celestial bodies. Capture scenarios have been proposed and studied as methods to potentially detect DM interacting with baryonic matter. These methods consider how DM interactions, such as scattering or annihilation/decay events, can deposit energy into an object such as a star resulting in internal heating. This thesis focuses on DM being captured by neutron stars. These are highly dense objects that result from the death of stars in the mass range of $10-25\,M_{\odot}$ [25]. We go further into key phases of a neutron star's evolution in Section 5.4. Our motivation for focusing on these objects lies in their extreme densities being ideal attractors of DM particles for capture and energy injection. We are also motivated by neutron stars having the highest sensitivity to the scattering cross section of all celestial objects. For sufficiently old stars, they will have cooled enough that the heating from kinetic energy being deposited can greatly influence their surface temperatures. We dive further into the physics of neutron star cooling in Section 5.4.

This section is structured as follows. We overview celestial objects that are used in studying DM capture while mentioning their benefits and drawbacks. We then describe the physics of how DM particles can be captured through scattering and their kinetic energy deposited to the object.

3.1 Relevant Bodies for Study

The best celestial body that can be used to potentially observe the effects of DM capture has been an important area of research. Bodies such as stars (e.g., main sequence, neutron stars), and Jupiter sized planets [20], have been of particular interest. These objects, along with many others, have their merits and downsides when it comes to DM capture. Leane and Tong (2024) [20] explore objects that can be used for studying capture, and provide observational benefits and drawbacks for future surveys.

Neutron Stars

Due to their high densities and large population [26], neutron stars are seen as ideal candidates for studying DM capture. Leane and Tong (2024) describe them as the most sensitive objects for small scattering cross sections, covering a majority of DM masses as seen in Figure 8. The primary drawback lies in the detection of old, cold neutron stars due to how small they are and how low their temperature is required to be to detect any significant DM heating.

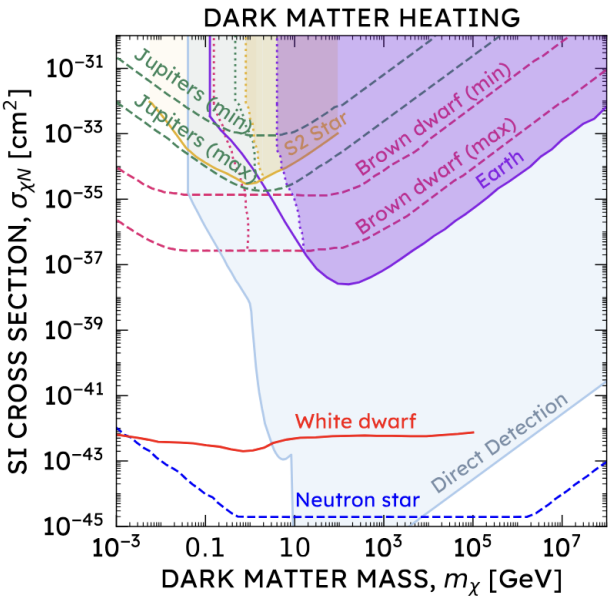

Figure 8: Scattering cross section for various celestial objects proposed for studying DM capture [20]. Dashed and solid lines represent the lowest constraints for the respective objects. Shaded regions indicate current bounds on cross sections from direct detection (blue shaded) and Earth DM capture experiments (purple shaded).

Main Sequence Stars

Main sequence stars have been considered for capture study due to their abundance and how accessible they are to observations. The concern with using them as DM probes is how hot they already are, meaning it is much more difficult to discern heating caused by DM energy injection from scattering or annihilation interactions. Leane and Tong (2024) state that they could still be viable targets if they are within high density DM regions, such as the galactic center.

Jupiter-like Exoplanets

Jupiter-like exoplanets provide the benefit of being easier to detect, with many exoplanet surveys already being cataloged with future missions proposed. The drawback in trying to locally detect DM heating within these objects is that the DM density is very low and would require large samples to discern any potential changes to their temperatures. Leane and Tong (2024) also outline the use of exoplanets in the Galactic bulge as candidates for observation due to the higher DM density in such a region.

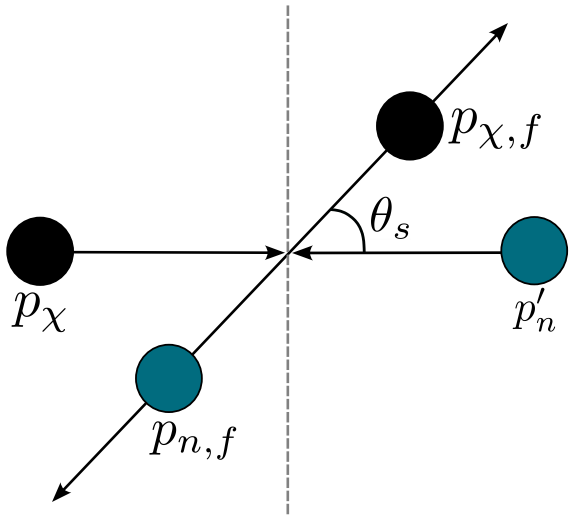

Figure 9: Visualization of DM-neutron scattering event in the center of mass frame. The initial momentum of the DM and neutron are denoted as p_χ and p'_n respectively. After scattering at angle θ_s, the particles have final momenta $p_{\chi,f}$ and $p_{n,f}$.

3.2 Physical Interactions Leading to Capture

In Section 2 we state our choice of $m_\chi = 100\,\text{GeV}$ for the DM particle mass. Here we outline the physics behind scattering interactions that allow us to consider this mass for a single-scatter capture scenario. A DM-nucleon scattering event causes the DM particle to lose kinetic energy it initially had. This energy lost by the particle is dependent on the mass of DM m_χ, the target (neutron) mass m_n, the velocity of the particle and escape velocity of the body (neutron star) v_{esc}, and the scattering angle θ_s in the center of mass frame [22, 27, 28];

$$\Delta E_\chi = \frac{m_n m_\chi^2 \gamma^2 v_{\text{esc}}^2}{m_n^2 + m_\chi^2 + 2\gamma m_\chi m_n}(1 - \cos\theta_s) \tag{3.1}$$

Where γ is the relativistic factor that we include due to the particle being boosted by the extremely dense neutron star. The full derivation of equation 3.1 is based on the calculation in Camargo et al. [28] and can be found in Appendix A.

Here we define m_n and m_χ to be the mass of the neutron and incident DM particle χ respectively. γ is the conventional Lorentz boost factor in terms of energy and momentum, and v_{esc} is the velocity required to escape the gravitational potential of the neutron star. For a neutron star of mass $M_{NS} = 1.5\,M_\odot$ and radius $R_{NS} = 10\,\text{km}$,

$$v_{esc} = \sqrt{\frac{2GM_{NS}}{R_{NS}}} \sim 0.66c \tag{3.2}$$

We include the derivation of the relativistic two-particle scattering, shown in Figure 9, in Appendix A that follows from [28]. The importance of equation (3.1) comes when we consider the kinetic energy of the incoming DM particle $KE_\chi = \frac{1}{2}\gamma m_\chi v_\chi^2$ with DM velocity $v_\chi \sim 230\,\mathrm{km/s}$, taken from the rotational velocity at the Sun's position in the Milky Way [29]. If the incoming particle has kinetic energy greater than the energy that would be lost from scattering with a neutron, then it will not be captured by the star. In this case, multiple scatters are required to ensure it is captured. Conversely, if the incoming energy is equal or less than the energy lost, then the particle will be captured after the first scatter. The upper mass limit can be defined by equating the energy loss ΔE_χ and the kinetic energy KE_χ [27, 22],

$$KE_\chi \leq \Delta E_\chi \tag{3.3}$$

Using equation (3.3) to solve for the upper mass bound for single scatter capture (determined when $1 - \cos\theta_s = 1$ in equation (3.1)) we get $m_\chi \sim 1\,\mathrm{PeV}$, consistent with that from Baryakhtar et al [22]. This means that multiple scatters are required to capture DM particles of $m_\chi \gtrsim 1\,\mathrm{PeV}$. Since we are considering WIMPs scattering with neutrons (eV-TeV mass range) we are well within the limits for single-scatter capture. We therefore move forward with the assumption that the DM particles scattering with neutrons do not require subsequent interactions to ensure capture.

3.3 General Formalism for Capture

When a DM particle encounters a celestial body such as a neutron star, they can undergo scattering interactions that cause them to lose kinetic energy and become captured gravitationally by the body. During the process, there are key considerations that factor into whether the particle will be captured by a given body. These include the density of DM that surrounds the celestial body as well as the interaction cross section between DM and Standard Model particles such as fermions. The rate at which this occurs is summarized as the capture rate,

$$C_\star = \underbrace{4\pi \int_0^{R_\star} r^2}_{\text{Volume of Star}} \underbrace{\int_0^\infty \frac{f(u)}{u} w\Omega_v^-(w)}_{\text{Particle Scattering}} \, du dr \tag{3.4}$$

This encapsulates how the size and mass of the star affects the ability to capture a particle of a given mass and inherent interaction cross-section. The scattering process that results in capture is dependent on the velocity distribution of DM, $f(u)$ where u is the DM velocity, and the lowering rate $\Omega_v^-(w)$. $\Omega_v^-(w)$ describes the rate

at which a DM particle will scatter to a lower velocity, losing enough energy to remain inside the star. This depends on the scattering cross section $\sigma_{n\chi}$ and the density of DM ρ_χ.

Our work follows the prescription of DM capture laid out in Baryakhtar et al. [22]. Here, they describe the kinetic energy deposited by DM in a neutron star which we will be using as the quantity governing kinetic heating in neutron star cooling (see Section 5.4).

$$\dot{E}_\chi = \frac{E_\chi \dot{m}}{m_\chi} f \tag{3.5}$$

Here we have $E_\chi = m_\chi(\gamma - 1)$ defined as the relativistic kinetic energy of the DM particles. The factor γ accounts for the near-relativistic velocity that DM experiences from being boosted by an encounter with a highly dense neutron star. In general, the boost factor can be computed for a given star mass and radius $M_\star$, $R_\star$ [23]:

$$\gamma = 1 + \frac{2GM_\star}{R_\star} \tag{3.6}$$

For our benchmark neutron star of mass $M_{NS} = 1.5\,M_\odot$ and radius $R_{NS} = 10\,\text{km}$, the boost factor is $\gamma \sim 1.4$. f is the fraction of DM particles that become captured and bound by the star, a quantity dependent on the interaction cross section. This quantity is defined as [22]:

$$f \equiv \text{Min}\left[\frac{\sigma_{n\chi}}{\sigma_{\text{sat}}}, 1\right] \tag{3.7}$$

where the saturation cross section σ_{sat} depends on the cross sectional area of the neutron star πR_{NS}^2, and the number of neutrons it contains $N_n = M_{\text{NS}}/m_n$.

$$\sigma_{\text{sat}} \simeq \frac{\pi R_{\text{NS}}^2}{N_n} = \frac{\pi R_{\text{NS}}^2 m_n}{M_{\text{NS}}} \simeq 2 \times 10^{-45}\,\text{cm}^2 \left(\frac{1.5\,M_\odot}{M_{\text{NS}}}\right)\left(\frac{R_{\text{NS}}}{10\,\text{km}}\right)^2 \tag{3.8}$$

The ratio $\sigma_{n\chi}/\sigma_{\text{sat}}$ signifies the probability that a DM particle will be captured. Intuitively, we can think of the neutron star as a net of neutrons, with σ_{sat} defining how much they are "bunched up" with each other. If σ_{sat} is larger than $\sigma_{n\chi}$ then this means all DM passing through the star will be captured ($f \gtrsim 1$). We note that this applies for the GeV $-$ PeV mass range in which DM is captured after a single scattering event, as described in the previous section. In contrast, if $\sigma_{n\chi}$ is less than σ_{sat}, then the probability of capture decreases [23]. We can vary $\sigma_{n\chi}$ so that $f \sim 1$, meaning that all dark matter passing through the body is captured.

Baryakhtar simplifies the capture rate of DM within a body down to the rate of DM mass passing through the body paired with the fraction captured.

$$\dot{m} = \pi b_{\max}^2 v_\chi \rho_\chi \tag{3.9}$$

The quantities here are the DM velocity, v_χ, the density of DM ρ_χ that the neutron star is placed in, and the maximum impact parameter $b_{\max}$ for a DM particle to be gravitationally captured by a neutron star [22]. $b_{\max}$ is therefore dependent on the mass M_{NS} and radius R_{NS} of the star, and the velocity of DM;

$$b_{\max} = \left(\frac{2GM_{NS}R_{NS}}{v_\chi^2}\right)^{1/2}\left(1-\frac{2GM_{NS}}{R_{NS}}\right)^{-1/2} \tag{3.10}$$

With these expressions defined, we will use the kinetic energy deposition rate $\dot{E}_\chi$ to solve the neutron star cooling curves in Section 5.4.

In this Section we went over how DM being captured in a celestial body, such as stars or exoplanets, can lead to energy deposited through scattering interactions. We have described the formalism surrounding this energy injection, particularly the kinetic heating rate in equation (3.5). We saw that it depends on the density of DM that the celestial body is subject to, through the mass rate in equation (3.9). This is where we will apply our key modification of considering DM substructure in the Milky Way as opposed to a typical smooth distribution.

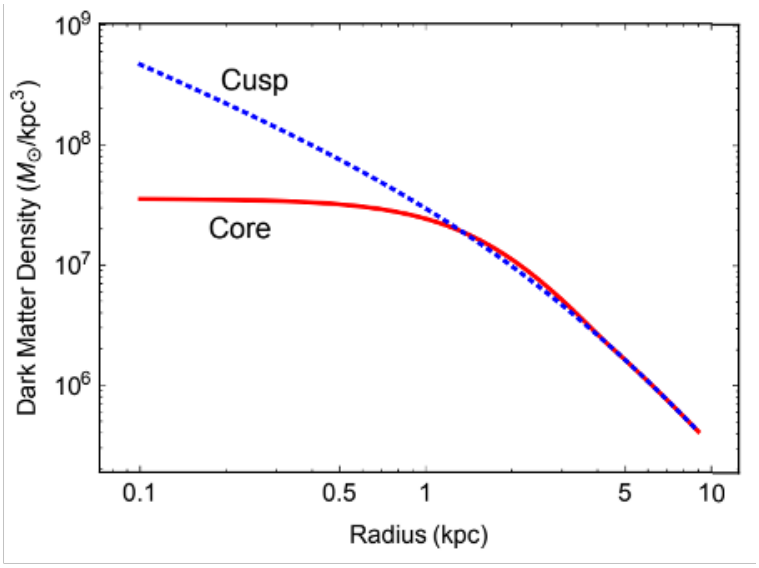

Figure 10: Core vs. cusp density profiles of DM halos from Tulin and Yu (2017) [30]. Cuspy halo density profiles are predicted by CDM N-body simulations, while observations show more cored profiles.

4 Dark Matter Capture from Clumpy Distributions

If we want to observe the effects of multiple halo impact capture, we need to evolve the body, e.g., the neutron star, within a region of the Milky Way (MW) and simulate encounters stochastically. This can be done by setting an encounter rate of halos for a given position R_{MW} in the MW (see Section 4.3). Each encounter the body has with a subhalo is kinematically determined by sampling distributions of the impact parameter $b_{\rm Imp}$ and the time between encounters $\tau_{\rm enc}$, which are defined by the halo radius $R_{\rm h}$ and mass $M_{\rm h}$. The distributions are outlined in Appendix B.

4.1 Cosmology of Dark Matter Substructure

Standard DM halos of galaxies are assumed to be smooth in their density distributions, i.e., neglecting the possibility of substructure on small scales. This is based off of CDM N-body simulations that predict galactic NFW-type halos, which have been accurate in describing the large scale structure of the Universe [19]. Despite the success at large scales, these simulations are unable to predict how DM behaves on the sub-galactic scale. This is notably seen in the core-cusp problem which has shown discrepancies between the predicted central regions of galactic halos using the NFW profile, and observations of low surface brightness (LSB) galaxies that are more. This discrepancy can be seen in the halo density plot in Figure 10. Due to their low surface brightness, these galaxies can probe the density profile more accurately by calculating their

rotation curves and observing how much DM contributes to their velocities compared to visible matter. This brings questions about the behavior of DM on small scales, which allows flexibility in exploring different structure formation models. One such possibility is that DM is composed of substructure, such as subhalos, on the sub-galactic level as opposed to the assumed smooth distributions that are generally considered.

The standard cosmological model sets the following evolutionary track; After the big bang, the Universe is radiation-dominated. Shortly after the Big Bang ($\sim 10^{-36}$ s), a period of rapid expansion occurs, known as inflation. Once inflation ends, the Universe returns to being radiation-dominated up to 0.05 Myr after the Big Bang. At this point, matter dominates the energy density of the Universe until 10.2 Gyr after the Big Bang. From here until the present, the Universe is dark energy (Λ) dominated. If we make changes to the early stages of the standard cosmology, we can introduce perturbations to DM densities in the early Universe that can result in DM substructures forming and persisting to the present epoch. We can consider two methods of early Universe substructure formation that remains consistent with large-scale CDM cosmology;

- **Early matter domination stage (EMD)** [31, 32, 33] By modifying assumptions to the standard cosmological model in the early Universe, we can introduce density perturbations that can make changes to the small-scale matter power spectrum. One such method is by introducing a scalar field that decays into radiation and DM particles prior to when the Universe becomes radiation dominated. Erickcek & Sigurdson [33] describe this decaying field as producing DM perturbations that yields early halo growth that leads to $> 50\%$ of all DM being confined to these compact structures in the present day.

- **Changes to initial conditions of inflation** [34]: An example of using inflation to result in substructure formation has been explored by considering an inflation model that allows for resonant particle production. Using a model that has an inflaton field ϕ coupled with a heavy scalar field φ, interactions between the two can result in perturbations to the inflaton field which can be seen on the power spectrum in Figure 11. This introduces the necessary corrections to the standard ΛCDM power spectrum required to produce DM substructure.

Our work makes the assumption that small-scale structure formation is possible and has resulted in a DM distribution primarily composed of substructures. The extent of subhalo number density and its effects on neutron star cooling is what we turn our focus to in the subsequent sections.

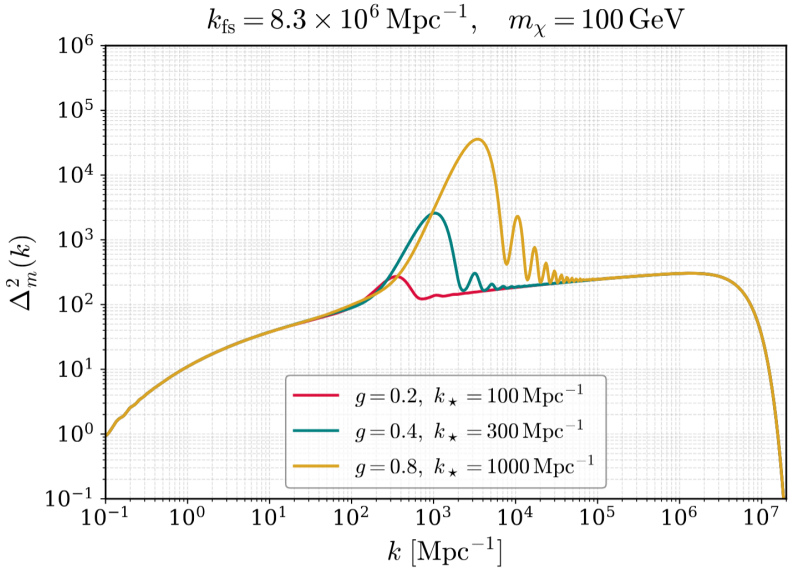

Figure 11: Small scale power spectrum from modifications to inflation [34]. These changes produce fluctuations at small scales that are not visible in the CMB power spectrum, allowing for consistency with CDM while producing DM substructure. The x-axis k^{-1} (scale) indicates the sizes of the substructure that can be present and the y-axis $\Delta_m^2(k)$ shows how many times more dense they can be with respect to the mean DM density (follows as $\sqrt{\Delta_m^2(k)}$ times more dense)

4.2 Subhalo Profiles

As mentioned previously, cold DM (CDM) provides an accurate model for large scale structure. The halos formed from a weakly interacting model can be described by the Navarro-Frenk-White (NFW) density profile [3],

$$\rho(r) = \frac{4\rho_s}{\left(\frac{r}{r_s}\right)\left(1+\frac{r}{r_s}\right)^2} \tag{4.1}$$

Other cored profiles, such as a Burkert profile, propose lower densities compared to NFW. We solely consider the NFW profile in our work, primarily due to the inner core of the halo not being an area of interest. We leave the exploration of varying density profiles to future study. The parameter r_s is the scale radius of the halo, defined as $r_s = R_h/c_*$, where R_h is the radius of the halo and c_* is the concentration parameter. Note that the standard relation is defined as $r_s = r_{200}/c_*$ where r_{200} is the virial radius of a halo of average density 200 times the background DM density. For our work, we take the virial radius to be the radius of the halo, $r_{200} = R_h$. The scale radius can be described as the radial position where the slope of the profile changes from the cusped inner core to r^{-3} in the outer region.

The characteristic density of the halo ρ_s, is a key parameter that we will be using in defining the density profile of the subhalos encountered by our benchmark neutron star. It is convenient to determine the density profile of a given halo based on its radius R_h and mass M_h. To do so, we will lay out a prescription in determining ρ_s to be used in equation (4.1). The expressions and quantity definitions used for NFW profiles are defined in Blinov et al. [35].

We begin by considering the scale mass M_s of the halo, which can be written in terms of R_h (through c_*) and M_h;

$$M_s = \frac{f(1)}{f(c_*)} M_h = 16\pi\rho_s r_s^3 f(1) \tag{4.2}$$

where the dimensionless functions $f(c_*)$ and $f(1)$ are defined as follows;

$$f(c_*) = \ln(c_*+1) - \frac{c_*}{c_*+1}, \qquad f(1) = \ln(1+1) - \frac{1}{1+1} = \ln(2) - \frac{1}{2} \tag{4.3}$$

The characteristic density can then be determined by rearranging equation (4.2) for ρ_s, giving an expression in terms of the halo mass M_h and radius R_h;

$$\rho_s = \frac{M_s}{16\pi r_s^3 f(1)} \tag{4.4}$$

We note that the impact parameter b governs how long the star spends in the halo, as well as the density it will profile it experiences. This can be seen this in Figure 12 where the density profile of the halo can vary depending on b_{Imp}, resulting in shallower profiles for larger impact parameters (farther from center) or more prominent peaks (closer to center).

4.3 Subhalo Encounters

Our simulation is designed to be stochastic to mimic the variability that could be present in realistic encounters. To show how this is implemented, we will now explicitly define the sampled parameters that help in defining the encounter history of neutron stars with subhalos. The two primary quantities are the impact parameter of the interaction b_{Imp}, and the time between encounters τ_{enc}. These define the extent of DM heating in the star and how frequently it interacts with DM subhalos. Here we will outline the specifics of subhalo encounters, touching on the rate of encounters and the path neutron stars take through a halo.

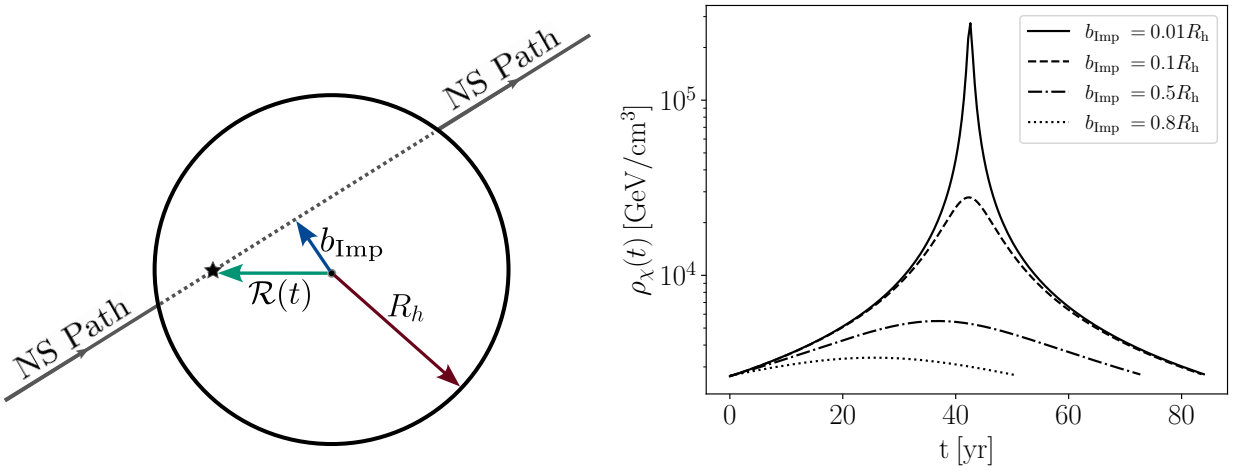

Figure 12: **Left:** Geometry of neutron star encountering a subhalo. The star follows a path (grey solid and dashed) defined by the impact parameter b with respect to the center of a halo of radius r_h. At any given time while inside the halo, the star is a distance $\mathcal{R}(t)$ from the halo center, defined in equation (5.11). During this time the star follows a chord path defined by b and r_h. As it traverses through, the position along the chord is defined by the angle θ between b and $\mathcal{R}(t)$. **Right:** Density profile for an NFW subhalo with respect to the time spent in crossing the halo. Curves indicate the density a star experiences as it passes through, dependent on the impact parameter $b_{\rm Imp}$. For larger $b_{\rm Imp}$, the density profile becomes shallower, depicting an encounter farther away from the center of the halo.

Encounter Rate

Between each encounter, the neutron star spends time in a region of negligible DM density. The amount of time it spends here is dependent on the rate of encounter of a given set of halo parameters (M_h, R_h). We define the encounter rate in terms of the subhalo number density per unit volume $n = \bar{\rho}_\chi / M_h$, the subhalo cross section σ_h, and the subhalo velocity v_h;

$$\Gamma_{\rm enc} = n\sigma_h v_h = \frac{\bar{\rho}_\chi}{M_h}\pi R_h^2 v_h \tag{4.5}$$

For a given halo mass and radius, this is a set quantity. This allows us to set a sampling distribution for the time between encounters $\tau_{\rm enc}$ as described in Appendix B. The encounter rate allows us to determine the number of impacts that a neutron star could theoretically encounter over a given period of time $\Delta t_{\rm Evo}$,

$$N_{\rm Enc} = \Delta t_{\rm Evo}\Gamma_{\rm enc} \tag{4.6}$$

We use equation (4.6) to plot the number of encounters $N_{\rm Enc}$ in the $(M_{\rm h}, R_{\rm h})$ plane over a period of 5 Gyr. This evolution time allows us probe lower encounter rates and impose a constraint of $N_{\rm Enc} \sim 1$ per 5 Gyr. This can be seen represented in the lower right corner in Figure 13. Due to the scarcity of encounters, the parameters

in this region are not considered in our simulations. We are also interested in subhalo encounters that are consistent with null results obtained from DD and ID experiments. We account for this by considering an upper bound to the frequency of one per $\sim 100\,\text{yrs}$. This corresponds to an encounter rate of $\Gamma^{+}_{\text{enc}} = 1/100\,\text{yr}^{-1} = 10^{7}\,\text{Gyr}^{-1}$. This is sufficiently large enough that our confined parameter space is not bound by our direct detection results, i.e., well outside of allowed constraints in Figure 13.

Geometry of Encounter

Since our case of study is based on how the clumpiness of DM can change the temperature evolution profile of a neutron star, we need to consider how these halos interact with them. In our simulations, the neutron star's encounter with a subhalo is based on two sampled parameters; the impact parameter b_{Imp}, and the time between encounters τ_{enc}. The probability distribution functions (PDFs) of b_{Imp} and τ_{enc} that are used for sampling follow a linear and exponential distribution respectively;

$$\text{PDF}(b_{\text{Imp}}) = 2b_{\text{Imp}} \tag{4.7}$$

$$\text{PDF}\,(\tau_{\text{enc}}) = \Gamma_{\text{enc}} \exp\left(-\Gamma_{\text{enc}}\tau_{\text{enc}}\right) \tag{4.8}$$

These distribution functions are further outlined in Appendix B. The impact parameter b_{Imp} is the distance of closest approach relative to the center of the halo, which defines the chord path the neutron star follows through the halo (Figure 12). For simplicity simulations, we keep the halo velocity constant across all encounters at $v_h \sim 233\,\text{km/s}$, i.e, the circular velocity at the radial position the Sun is located in the Milky Way. We note that our simulation can be modified to take the halo velocity from a distribution for future studies.

For each encounter, the impact parameter is sampled and assigned such that the path through the NFW halo can be determined for an accurate density calculation. As the star traverses through the halo, the DM density at a given position is calculated using the re-parameterized NFW profile in equation (5.12)

4.4 Clumpiness of Distribution

If we consider the Milky Way halo to have substructure rather than being completely smooth, then we can study the effects of how different subhalo encounters could observably affect neutron stars. To do so, we

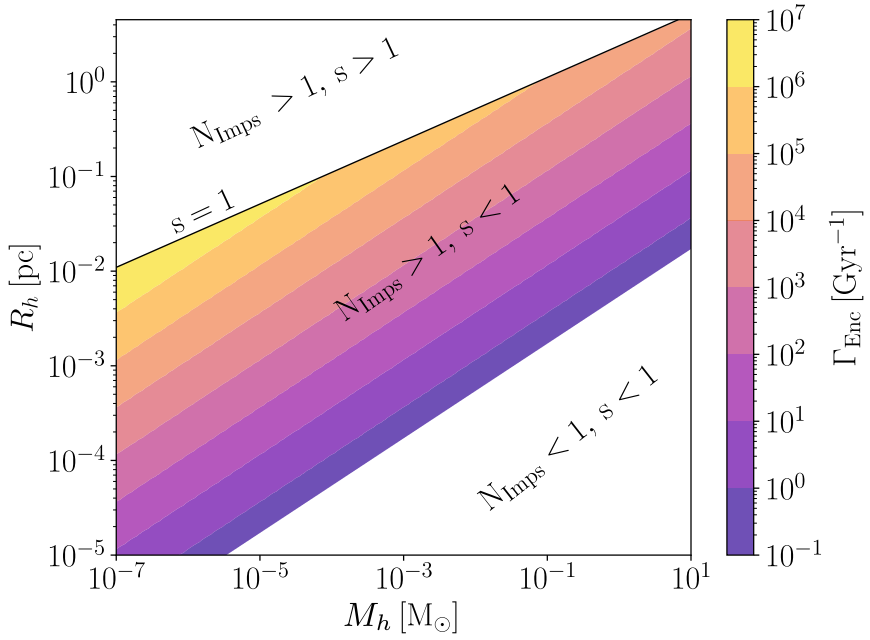

Figure 13: DM subhalo parameter space (M_h, R_h) depicting the encounter rate $\Gamma_{\rm Enc}$ used in the sampling distribution of the time between encounters $\tau_{\rm enc}$. The parameters in the colored region are what we use in our simulations. We also define the smoothness parameter s which we use as an indicator for how "clumpy" the galactic halo is at the local position. We define $s = 1$ to be the transition from clumpy to smooth, i.e., the maximum time spent crossing a subhalo of radius R_h at velocity v_h is equal to the encounter rate $\Gamma_{\rm Enc}$.

define a parameter that quantifies the smoothness of the Milky Way halo, s;

$$s = \Delta t_{\rm cross}(R_h, v_h)\Gamma_{\rm enc} = \frac{R_h}{v_h}\left[\frac{\bar{\rho_\chi}(R)}{M_h}\pi R_h^2 v_h\right] \propto \frac{R_h^3}{M_h} \tag{4.9}$$

$$s = \begin{cases} \ll 1 & \text{Clumpy Distribution} \\ \gg 1 & \text{Smooth Distribution} \end{cases} \tag{4.10}$$

Here we can quantify how clumpy the halo is depending on the position of the Milky Way we are at (through $\bar{\rho_\chi}(R)$), and physical and kinematic parameters of the DM subhalo that is considered, r_h, M_h and v_h.

When $s > 1$, the time it takes to cross a subhalo $\Delta t_{\rm cross}$ is comparable to $\Gamma_{\rm enc}^{-1}$, i.e., $\Delta t_{\rm cross} \simeq \Gamma_{\rm enc}^{-1}$. This means that before exiting the halo, you are likely to encounter another subhalo right away, meaning the act of entering the next halo immediately is equivalent to remaining a smooth distribution. When $s < 1$, the time it takes to cross a subhalo is less than the time between encounters. This means that the neutron star spends a non-zero amount of time outside of a halo. Figure 13 shows subhalo parameters consistent with a clumpy distribution and that provide at least a single encounter over a period of 5 Gyrs.

By considering DM to have inherent clumpiness in its distribution, we allow ourselves to loosen constraints imposed by direct detection experiments. If we assume that Earth has not encountered a subhalo since at least when detection experiments began in the 1980s [19], we can continue to allow larger interaction cross sections when exploring various particle models of DM. Our work takes all DM to be confined to within galactic substructures, with no smooth component. We note that there are hierarchical models, as considered Mao et al. [36], which combine substructure and smooth components for a cumulative DM distribution. We next move to describe how neutron stars can be used as DM laboratories. We focus on the effects caused by energy deposited from DM-nucleon particle scattering from multiple subhalo encounters with these compact bodies. This energy injection can change the temperature of these objects which could potentially be detected by modern or next-generation telescopes. With a large enough sample size of neutron stars, we can determine the likelihood of a neutron star being affected by DM subhalos, allowing us to apply constraint independent of DD and ID experiments.

5 Neutron Stars as Dark Matter Laboratories

In Section 3 we describe the mechanism for the capture of a DM particle in neutron stars through scattering interactions with neutron targets. In this Section we overview how neutron stars can be used as DM probes through dark kinetic heating effects. Section 5.2 reviews previous studies that focus on DM scattering in neutron stars, providing potentially observable impacts to their temperatures. In Section 5.3 we briefly describe DM thermalization, specifically noting the time scale at which 99% of the energy from scattering interactions is deposited. We see that this is essentially instantaneous on stellar evolution time scales. Section 5.4 reviews the processes governing neutron star cooling, outlining the three primary phases that culminates in photon emission which is the main mechanism after 10^5 yrs. We also present the ODE that describes the cooling evolution of a star that it affects by dark kinetic heating and photon emission. Lastly, we overview the density profiles we use for the DM subhalos, presenting the uniform density and NFW profile that we use in evaluating the ODE.

5.1 Neutron Star Formation and Structure

Toward the end of the lifecycle of massive stars $M > 8\,M_\odot$, they continue to burn carbon and oxygen in their cores. Smaller mass stars will end their lives as white dwarfs, shedding off their outer layers to reveal a degenerate carbon-oxygen (CO) core. But stars of sufficient mass will continue to burn, increasing in core mass toward the Chandrasekhar limit. This build up of density causes multiple burning shells until an iron core is formed. Since iron cannot be efficiently fused, the cycle of burning shells ends, causing the iron core to increase in mass until it reaches the Chandrasekhar limit. Once it exceeds this limit the electron degeneracy pressure can no longer oppose gravity causing the star to collapse as a Type II supernova [37]. This continues until equilibrium is reached between nucleons in the core and the extreme density of the newly formed neutron star. For sufficiently massive stars ($> 20\,M_\odot$), this collapse does not stop, leading to a singularity (i.e., a black hole).

The internal structure of a neutron star is composed of two primary regions; the crust and the core.

After collapse, these stars have extremely high internal temperature, around $\sim 10^{11}$ K. This is due to the high density of the core and the presence of a heat-blanketing envelope, composed of lighter elements such as H and He, that insulates the inner regions of the star [38]. This results in a temperature gradient between the surface and the inner boundary of the envelope $T_s - T_b$. For sufficiently old stars ($\sim 10^7$ yrs), this envelope is

thin enough such that $T_s \simeq T_b$ [38]. This means that for old, cold neutron stars, T_s is indicative of temperature inside the star.

5.2 Previous Studies of Neutron Star Kinetic Heating

Dark kinetic heating in neutron stars has been explored and continues to be an active area of research due to being ideal probes for scattering cross-sections. Work by Baryakhtar et al. (2017) and Bramante et al. (2023) [22, 39] explore the affects of DM if a neutron star is present in a smooth or substructured density distribution, similar to the work in this thesis.

Baryakhtar et al. (2017) provides a framework for detecting effects of DM kinetic heating in neutron stars by determining their minimum temperature under such a process. Under the blackbody assumption, they present the spectral flux density that the stars would emit due to kinetic heating (for a temperature of 1750 K). Their results conclude a flux density of ~ 0.5 nJy (nanoJansky), which could potentially be detected using future telescopes.

Bramante et al. (2023) considers a scenario similar to the work we are presenting in this thesis. Assuming the Milky Way DM halo is composed of substructure, a neutron star can be kinetically heated whenever it encounters a subhalo. Their motivation, similar to ours, is based on the lack of signals from DD experiments. They present calculations on the energy deposited by DM scattering, which result in increased luminosities that could be probed with next generation telescopes. These luminosity calculations are evaluated for "frequent" and "infrequent" encounters.

This thesis builds on the work these studies have presented by considering a substructure DM distribution and developing a stochastic simulation of a neutron star encountering subhalos. This allows us to study the clumpiness of a distribution in a more continuous manner (spanning over various subhalo number distributions), dependent on the halo masses and radii. This also provides a detailed evolution history of a neutron star's temperature that can vary due to our introduction of stochasticity.

5.3 Neutron Star Thermalization

When DM particles become gravitationally bound to a body such as a neutron star, they will continue to lose energy as they scatter with target particles (neutrons) [40]. The particles will eventually reach a thermal equilibrium in the star, forming a DM core with radius [41]. The size of this core is not an area we study, but it could hold an interesting area of research when considering the dynamics of a changing DM core from

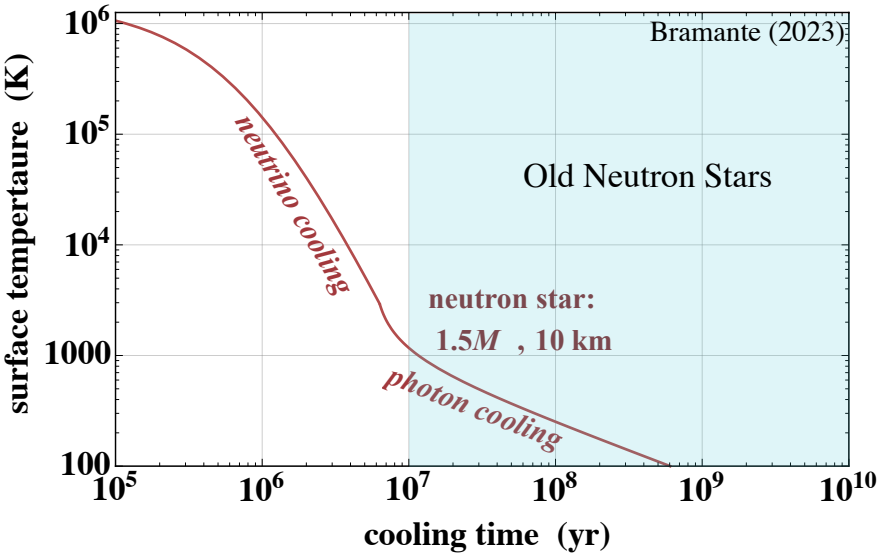

Figure 14: Cooling curve of neutron star after its proton-neutron star phase [42]. Prior to $\sim 10^7$ yrs cooling is dominated by neutrino emission. As it continues to cool, this phase becomes subdominant to photon emission from the surface. This is defined by the shaded blue region $\gtrsim 10^7$ yrs.

our multiple halo encounter scenario. The time scale to which thermalization occurs depends on the DM mass and particle model being considered. In section 2 we described the O_1^F EFT operator we use as our toy model, which is the simplest fermionic model that scales as t^0 with respect to its Mandelstam variables. Our work considers kinetic heating of DM as the primary energy injection. Work from Bell et al. [40] shows that 99% of kinetic energy is deposited on the timescale of days, essentially instantaneous on stellar evolution scales.

5.4 Neutron Star Cooling

Neutron stars are born from supernovae of stars with an initial mass in the range of 10-25 $M_\odot$ [25]. The NS has a brief proto-neutron star phase in which it is opaque to neutrinos resulting in high internal temperatures on the order of $\sim 10^{11}$ K. Yakovlev and Pethick [38] describe the three primary phases of neutron star cooling:

1. **Thermal Relaxation**: Very brief stage, lasting $t < 10 - 100$ yrs in which the neutron star crust is thermally decoupled from the core, cooling at different rates [43]. On cosmological timescales, this stage occurs instantaneously.

2. **Neutrino Cooling**: Lasts for $t < 10^7$ yrs. Cooling at this stage is governed by neutrino emission from the core [38] (See Figure 14). This process continues until the temperature has dropped sufficiently to

allow photon emission to dominate cooling.

3. **Photon Cooling**: The remainder of cooling is governed by this stage, lasting from $t > 10^7$ yrs and driven by black-body photon emission from the surface. The extent of cooling is sensitive to the properties of the outer regions of the neutron star [43].

The reason cooling from photon emission eventually dominates over neutrino emission is due to the emissivities in the two processes. Neutrino emissivity depends strongly on the temperature of the neutron star, following as $\varepsilon_\nu^{\text{direct}} \propto T^6$ or $\varepsilon_\nu^{\text{slow}} \propto T^8$, depending on the neutrino production model considered [39, 44]. The two common neutrino production methods are the direct Urca process $(n \to p + e^- + \bar{\nu}_e)$ and the slow Urca process $(n + n \to p + e^- + \bar{\nu}_e)$. Regardless, both processes result in a larger temperature dependence than photon emission $\varepsilon_\gamma \propto T^4$. This means that as the temperature of the neutron star cools, the cooling contribution from neutrino emission will drop fast and eventually be subdominant to photon emission. We can see this in Figure 14 where neutrino emission dominates first 10^5 yrs, after which we see a drastic change in the cooling curve slope where photon emission takes over.

The full evolution of cooling follows from the first law of thermodynamics. The total energy of the system (neutron star) is affected by the energy leaving the system through cooling processes and the energy being put into it via heating sources.

$$\Delta E_{\text{total}} = Q_{\text{Heat}} - Q_{\text{Cool}}$$

Differentiating with respect to time gives the rate at which the energy changes;

$$\dot{E}_{\text{total}} = \dot{Q}_{\text{Heat}} - \dot{Q}_{\text{Cool}}$$

For a neutron star, after thermal relaxation, it undergoes cooling due to neutrino and photon emission. If the star experiences any reheating processes, they will work against these cooling processes [38]. Since we primarily consider cold and old neutron stars, the main contributors at this phase of their life cycles will be photon emission, along with any reheating contributions. Baryakhtar et al. [22] describes a simplified form of neutron star cooling that considers the heat capacity of the neutron star c_v, photon emission, denoted as the photon emissivity ε_γ, counteracted by kinetic heating from DM and accretion of interstellar matter (ISM),

denoted as ε_χ and $\varepsilon_{\rm ISM}$ for DM and ISM emissivities respectively.

$$\frac{dT}{dt} = \frac{\varepsilon_{\rm ISM} + \varepsilon_\chi - \varepsilon_\gamma}{c_v} \tag{5.1}$$

The solution to this ODE is commonly referred to as the cooling curve for neutron stars. In their work, they describe present-day ISM heating to be subdominant to heating from DM, with an ISM density of $\sim 10^{-3}\,\mathrm{GeV\,cm^{-3}}$ (in the local region of the Milky Way). Therefore, we can neglect any contributions to heating apart from that due to DM scattering, while keeping photon emission. This further simplifies the ODE in equation (5.1) to the following form:

$$\boxed{\frac{dT}{dt} = \frac{\varepsilon_\chi - \varepsilon_\gamma}{c_v}} \tag{5.2}$$

Cooling Curve Emissivities

The emissivities considered in equation (5.2) quantify how efficient the heating or cooling process is at transferring energy into or out of the system. For the DM heating and photon cooling processes, the emissivities have the following analytical form [22];

$$\varepsilon_\chi = L_\chi^\infty \times \frac{1}{V_{NS}} = \dot{E}_\chi \left(1 - \frac{2GM_{NS}}{R_{NS}}\right) \times \frac{1}{V_{NS}} \tag{5.3}$$

$$\varepsilon_\gamma = L_\gamma^\infty \times \frac{1}{V_{NS}} = 4\pi\sigma_{SB} R_{NS}^2 T^4 \left(1 - \frac{2GM_{NS}}{R_{NS}}\right) \times \frac{1}{V_{NS}} \tag{5.4}$$

We define M_{NS} and R_{NS} as the neutron star mass and radius respectively, V_{NS} as its volume, and σ_{SB} is the Stefan-Boltzmann constant. The DM and photon emissivities are described by their corresponding luminosity contributions, denoted by L_χ^∞ and L_γ^∞ respectively. These are the luminosities that would be seen by a distant observer, arising because of immense gravity near the neutron stars red-shifting the light as it escapes. DM luminosity is governed by the DM kinetic heating rate, $\dot{E}_\chi$, which is described in equation (3.5).

Neutron Star Heat Capacity

For simplicity, we consider our benchmark neutron star to be a spherical body with constant volume, primarily composed of neutrons, with negligible fractions of protons and electrons. The heat capacity c_v of such a star can be expressed in terms of the neutron mass m_n, the neutron number density of the star n_n, the Fermi

momentum for the neutrons $p_{F,n} = \hbar \left(3\pi^2 n_n\right)^{1/3}$, and the temperature of the star T. The Fermi momentum is required due to the extreme densities in neutron stars, meaning the Pauli exclusion principle affects the quantum states that the neutrons occupy. The specific heat capacity at constant volume c_v is dependent on the temperature of the star, and can then be written as follows [45];

$$c_v = \frac{2\pi^2 k_B^2 m_n n_n}{3p_{F,n}^2} T = \beta T \tag{5.5}$$

Note that a complete prescription of c_v considers the sum of the degenerate components (neutrons + electrons + protons), but we assume the star is composed of a degenerate neutron fluid for simplicity. In equation (5.5) we absorb the constants into β for compactness in our numerical solutions. If we consider benchmark neutron star of mass $M_{NS} = 1.5\,\mathrm{M}_\odot = 1.67 \times 10^{57}\,\mathrm{GeV}$ and radius $R_{NS} = 10\,\mathrm{km}$, the neutron number density n_n can be calculated as follows;

$$n_n = \frac{M_{NS}}{m_n V_{NS}} = \frac{1.67 \times 10^{57}\,\mathrm{GeV}}{0.939\,\mathrm{GeV}\left(\frac{4}{3}\pi\,(10^4\,\mathrm{m})^3\right)} \simeq 4.25 \times 10^{44}\,\mathrm{m}^{-3} \tag{5.6}$$

This yields a Fermi momentum of $p_{F,n} \simeq 0.45\,\mathrm{GeV}$. The value of β can then be computed as;

$$\beta = \frac{2\pi^2 k_B^2 m_n n_n}{3p_{F,n}^2} = 2.945 \times 10^{19}\,\mathrm{GeV\,m^{-3}\,K^{-2}} \tag{5.7}$$

The specific heat capacity in equation (5.5) can then be expressed numerically with temperature dependence as follows;

$$c_v \simeq (2.945 \times 10^{19}\,\mathrm{GeV\,m^{-3}\,K^{-2}}) \times T \tag{5.8}$$

With c_v defined for our benchmark star, we can begin applying equation (5.2) for different cases of subhalo density profiles.

Neutron Star Cooling Curves

Given the ODE in equation (5.2), we can solve for the cooling curves of a neutron star with respect to time. Our thesis uses this ODE to calculate the temperature evolution of a benchmark neutron star as it encounters multiple DM subhalos. To do this, we must consider the DM density that the star experiences during each encounter. Our two primary cases are uniform density halos and halos that follow the NFW

profile in equation (4.1). To provide confidence in our numerical solver, we derived the solution equation (5.2) for a uniform density halo, and for a toy model profile that depends on the position of the star. This toy model is a simple parabolic density function, parameterized by the halo radius R_h, and a scale density ρ_h that defines the profile peak. The motivation behind deriving the toy model solution is to confirm the accuracy of our solver when solving DM densities that vary with time.

$$\rho_\chi = \frac{3M_h}{4\pi R_h^3} \tag{5.9}$$

$$\rho_\chi(r) = \rho_h\left(1 - \frac{r^2}{R_h^2}\right) \tag{5.10}$$

Equation (5.9) represents the uniform mass density for spherical body of mass M_h and radius R_h, and equation (5.10) is the parabolic profile. We numerically and analytically solve the ODE for these two mass densities and plot how they compare with each other. The analytical solutions can be found in Appendix C. We see in Figure 16, the numerical and analytic solution agree with each other, allowing us to confidently use our numerical solver to evaluate equation (5.2) using an NFW profile. Before we describe our simulation, we must perform a reparameterization of the standard NFW profile to be explicitly dependent on time.

Cooling Curve with NFW Profile

With the confidence from our previous cooling curve examples, we move forward to lay the basis for numerically solving the cooling curve with an NFW density profile. To set up our numerical solver, we must make a change of variables for the profile. Recall in equation (4.1) we defined the NFW density profile:

$$\rho(r) = \frac{4\rho_s}{\left(\frac{r}{r_s}\right)\left(1+\frac{r}{r_s}\right)^2}$$

Since this is parameterized in terms of radial distance r from the center of the halo, we need to reparameterise in terms of time t for ease of simulating the curves, i.e., $r \to v_h(t - t_{\text{enter}})$. Here we define t_{enter} as the time at which the star has entered the halo. We consider the star to follow a chord through the halo, which is defined by an impact parameter b. Since the typical sizes for subhalos we are considering are much larger than the radius of the neutron star ($R_h \gg R_{NS}$), we can make the approximation that the star acts as a point particle in the halo from a geometry point of view. At any point along this path, the star will be a distance $\mathcal{R}(t)$

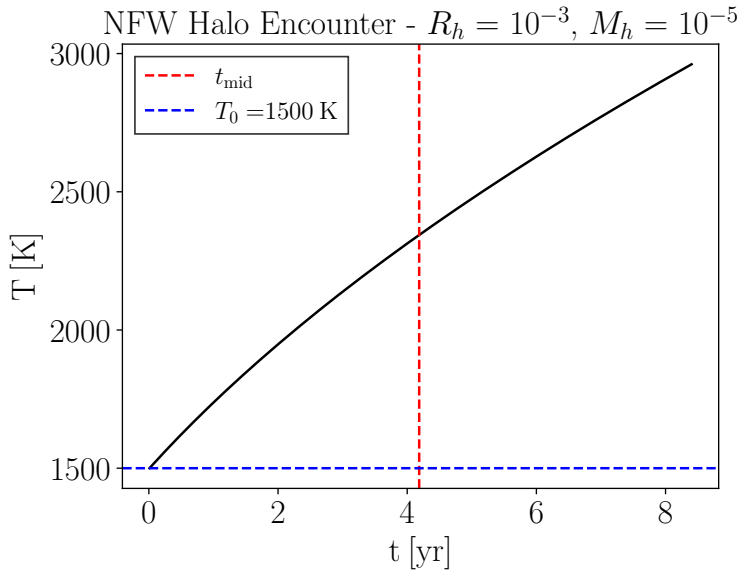

Figure 15: Cooling curve (black solid line) of a neutron star with an initial temperature of $T_0 = 1500\,\mathrm{K}$ (blue dashed line) as it encounters an NFW subhalo of mass and radius $M_h = 10^{-5}\,\mathrm{M}_\odot$ and $R_h = 10^{-3}\,\mathrm{pc}$. The red dashed line signifies the midpoint of encounter $t_{\rm mid}$.

from the center of the halo (see Figure 12). To account for this and for the fact that the star is traveling the full chord path, we consider the midpoint time $t_{\rm mid}$ where the star is at the midpoint of the chord path it is traveling along. The reparameterization can then be expressed in terms of the halo velocity v_h, the time the star enters the halo $t_{\rm enter}$, and the midpoint time $t_{\rm mid}$;

$$r \to v_h(t - t_{\rm enter}) \to v_h\left[(t - t_{\rm enter}) - t_{mid}\right]$$

Since the NFW profile is a non-uniform density profile, the position a star interacts with it is extremely relevant. We include this in our re-parameterization as the impact parameter b. All together, the re-parameterization takes the following form:

$$r \to \mathcal{R}(t) \equiv \sqrt{v_h^2\left[(t - t_{\rm enter}) - t_{mid}\right]^2 + b^2} \tag{5.11}$$

Figure 12 visualizes what $\mathcal{R}(t)$ represents physically with respect to the neutron star position and the center of the halo. The NFW density profile we will use moving forward now has the following form:

$$\boxed{\rho_\chi(t) = \frac{4\rho_s}{\left(\frac{\mathcal{R}(t)}{r_s}\right)\left(1 + \frac{\mathcal{R}(t)}{r_s}\right)^2}} \tag{5.12}$$

where we have $r_s = R_h/2$ and ρ_s follows from equation (4.4). Figure 15 shows an example cooling curve for a neutron star encounter with a subhalo of mass $M_h = 10^{-5}\,M_\odot$ and radius $R_h = 10^{-3}$ pc.

5.4.1 Time Spent at Elevated Temperature

To get a better idea of how kinetic heating from DM can affect neutron stars, we consider how much time they spend at elevated temperature. Since the interactions of DM with the NS result in the temperature increasing, we would expect to observe them at higher temperatures than that expected of old and cold neutron stars. To study this, we consider the NS cooling curve ODE in the case of no DM emissivity, i.e., photon emission is the only component that affects the temperature when outside of a halo.

In the absence of a heating source, e.g., ISM or DM, a neutron star will continue to cool through photon emission from its surface (See Section 5.4). Analytically, this is described by simplifying the ODE in equation (5.2) to a single term;

$$\left(\frac{dT}{dt}\right)_\gamma = -\frac{\varepsilon_\gamma}{c_v} = -\kappa T^3 \tag{5.13}$$

where we define κ to be a proportionality constant composed of terms from the photon emissivity ε_γ and heat capacity c_v;

$$\kappa = \frac{4\pi\sigma R^2}{\beta V_{NS}}\left(1 - \frac{2GM}{R}\right), \qquad [\kappa] = \mathrm{K}^{-2}\mathrm{s}^{-1} \tag{5.14}$$

where β is defined in equation (5.7). The ODE in equation (5.13) can be solved analytically and has the following form;

$$T_f = \frac{T_i}{\sqrt{2T_i^2\kappa\Delta t_{cool} + 1}} \tag{5.15}$$

Δt_{cool} is the time it takes for the NS to cool from an initial temperature T_i to a final temperature T_f. The full derivation of equation (5.15) is outlined in Appendix C.

In this Section we reviewed how neutron stars can be used to probe DM through the change in temperature caused by the energy deposited by scattering interactions (equation (5.2)). For defined density profile of DM subhalos, we can see an increase in temperature over a short period of time. In the next Section we outline our method for numerically solving equation (5.2) using our benchmark neutron star undergoing multiple encounters with uniform and NFW density subhalos.

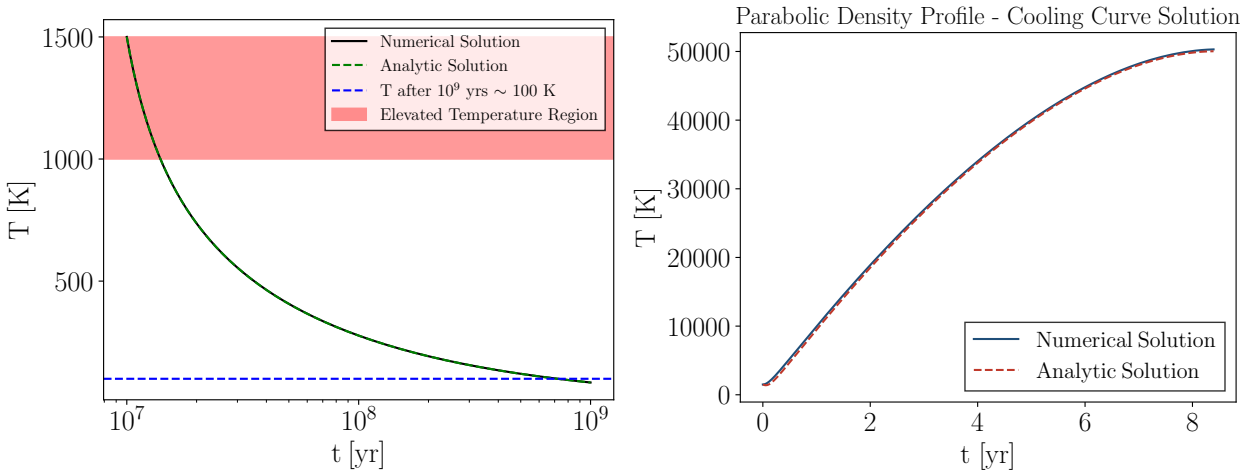

Figure 16: **Left:** Cooling curve of a neutron star that experiences photon emission and no heating. We use our benchmark star of mass $M_{NS} = 1.5\,M_\odot$ and radius $R_{NS} = 10\,\text{km}$ and numerically solve the ODE in equation (5.13) from $10^7 - 10^9$ yrs. At 10^9 yrs, with no external heating, a neutron star is predicted to be cooled down to a temperature of $\sim 100\,\text{K}$ [38]. **Right:** Cooling curve of a neutron star traveling through a halo with parabolic density profile as defined in equation (5.10). We see the solutions from our numerical solver (solid blue curve) and the analytic solution (dashed red line), outlined in Appendix C.3, are is strong agreement with each other.

6 Numerical Solutions to Neutron Star Cooling Curves

As described in Section 5.4, cooling curves for old, cold neutron stars will depend on photon emission as the primary source of heat dissipation. In the presence of a DM distribution, these cold neutron stars are kinetically heated by DM elastically scattering with neutrons. This process is described in equation (5.2). Previous studies explored the effect of dark kinetic heating from smooth distributions [22, 42, 20, 23]. Results indicate potentially observable increases in neutron star temperatures due to DM [22] which can potentially be explored as telescopes continue to improve in sensitivity. Our work builds on these past studies by considering DM substructure as the driver for dark kinetic heating.

This Section provides an overview of our simulation used to calculate the cooling curve (temperature profile) of our benchmark neutron star for multiple encounters with uniform and NFW density profile subhalos. The flow of our code is as follows;

1. A complete history of subhalo encounter histories is determined for a range of subhalo radii and mass (r_h, M_h). These ranges are defined by the allowed parameter space bounds seen in Figure 13. The encounter histories take note of each encounter event, logging the time spent in regions between and within halos.

2. Encounter histories are then used to numerically solve the ODE in equation (5.2) for the neutron star

cooling curves, using an NFW halo density profile. The star starts at an initial temperature of 1500 K, consistent with predicted old, cold stars after 10^7 yrs [38]. Here we obtain the neutron star temperature over a period of 5 Gyr, or until 500 encounters occur. Our choice of 5 Gyr was made to remain consistent with the hypothesized average age of old neutron stars in the Milky Way galaxy [26]. These old neutron stars are thought to be extremely abundant, albeit difficult to observe.

3. After the cooling curves are calculated, they are used to analyze the mean temperature during the simulation $\bar{T}$, the standard deviation of mean temperature $\sigma_{\bar{T}}$, and the fraction of time spent at an elevated temperature f_{elev}.

We will touch on each point of the simulation process from a technical perspective, outlining the approximations/assumptions made for our solver.

6.1 Cooling Inside and Outside of Halos

When outside of a halo, the cooling curve of the neutron star is governed only by photon emission, as seen in equation (5.13). The time spent in this phase is determined by sampling the encounter history of a given subhalo parameter set, as described in Section 6.2. The curve of this phase can be seen in Figure 16. Here we designate 1000 K to be the threshold for when the star is considered elevated in temperature.

Within a halo, the star is affected by dark kinetic heating. Here, photon emission is still present but is subdominant, with the cooling curve being described by DM and photon emissivities in equation (5.2). Time spent in this region is very small, on the order of years, due to the sizes of the halos and their velocity, taken to be 233 km/s.

6.2 Generating an Encounter History

As discussed in Section 4.3, each individual subhalo encounter is parameterized by the time between encounters τ_{enc} and the impact parameter b_{Imp}. Extending to multiple encounters, these quantities are used to define a complete encounter history that a neutron star experiences. To determine this history, we developed a simulation that takes in a given value for the evolution time, e.g., 5 Gyr, and a subhalo encounter threshold N_{Thresh}. N_{Thresh} is used to place a cap on the simulation time. If this threshold is reached before the end of the simulation time, we cut off the simulation here and take the encounter history in the limited time to be in-

dicative of the remainder of the evolution time. This is done to save on computation time for high encounter rate parameter sets.

Each simulation is initialized with a neutron star outside of a DM halo. After some time, the star encounters the first halo. At this moment the impact parameter is sampled from a predefined distribution and used to determine the chord path that the neutron star will take through the halo. This path is used to then calculate the distance from the center of the halo that the star will be at a given moment in time (see equation (5.11)). The time spent on the path is saved as an array. Once the star exits the halo, the time to the next encounter, $\tau_{\rm enc}$, is sampled to determine the time the star will spend outside of the halo until its next encounter. This process is then repeated until either the simulation time or encounter threshold $N_{\rm Thresh}$ are reached. We show an example of the cooling curves and encounter history for a subhalo mass and radius set of $(M_{\rm h}, R_{\rm h})$=$\left(5\times10^{-3}\,{\rm M}_\odot, 10^{-3}\,{\rm pc}\right)$.

Once the encounter history is generated, the full time evolution that was recorded is fed into the numerical solver to calculate the star's temperature. This solver uses equation (5.2) and iterates through the encounter history, designating phases within the halo and between encounters. Figure 17 visualizes the cooling curve for a neutron star for an encounter history of a subhalo parameter set of mass $M_{\rm h} = 5\times10^{-3}\,{\rm M}_\odot$ and radius $R_{\rm h} = 10^{-3}\,{\rm pc}$ resulting in 10 encounters in 5 Gyrs. We see for each encounter, the neutron star temperature increases dramatically over a period of ~ 10 yrs to temperatures of order 10^4 K while inside the halo (see lower panel of Figure 17. Upon exiting, photon emission quickly takes over, eventually cooling the star to temperatures of order 10^2 K.

6.3 Subhalo Parameter Space

With a generated encounter history, we solve the cooling curve of a neutron star for parameter sets that lie in the bounds of the parameter space shown in Figure 13. Previously we noted that for high encounter rate parameters, i.e., $s \sim 1$, computation times can increase drastically (Section 6.2). To limit this, we impose an overall limit of 500 encounters over the simulation time (if the simulation time is not reached before $N_{\rm Imps} = 500$ is reached). This allows us to probe parameters closer to a smoothness parameter of $s = 1$. For any values larger than that, the distribution enters into the smooth density regime and therefore parameters in this region are not considered (See Figure 13). Note that for simplicity, the internal evolution of the neutron star is considered static from the moment it reaches photon emission.

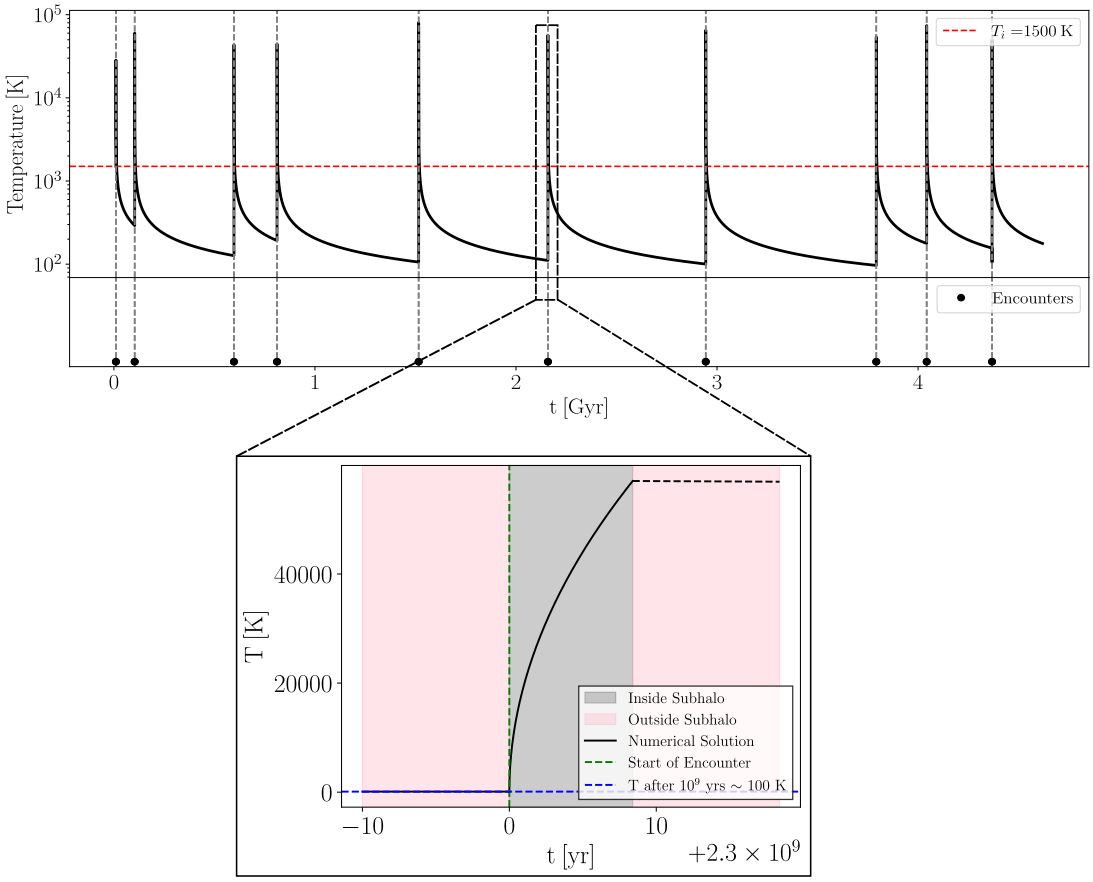

Figure 17: **Top:** Example encounter history and cooling curves for our benchmark neutron star with an initial temperature of 1500 K. Encounter history was produced from a uniform density subhalo of mass $M_{\rm h} = 5 \times 10^{-3}\,{\rm M}_\odot$ and radius $R_{\rm h} = 10^{-3}$ pc. Evolution begins at 0.01 Gyr and evolves until a simulation time of 5 Gyr or until 500 encounters are reached. Note that the cooling curves shown here only visualize the temperature between encounter due to the temperature spikes within halos happening on the timescale of yrs. **Bottom:** Zoomed-in visualization of the cooling curve during a subhalo encounter (gray shaded region), with extensions before and after the encounter (pink shaded regions). Before entering the halo, the star has been cooled to a temperature of $T \sim 100\,{\rm K}$. We then see the temperature increases substantially, on the order of 10^4 K, in a short period of time (~ 8 yrs) while inside the halo. After the encounter the star begins cooling through photon emission causing the temperature to drop until it encounters another subhalo.

6.4 Numerically Solving Neutron Star Cooling Curves

Throughout the encounter history, the star experiences regions of high DM density (within a halo), and no DM density (between encounters). While inside the halo, we must solve for the temperature in a fine grained manner since we also consider an NFW profile that is dependent on the position the star is located. This is done by numerically solving the cooling curve in equation (5.2) at multiple time steps to accurately capture the temperature change the star experiences. Upon leaving the halo, the neutron star is no longer being heated by DM particles depositing their kinetic energy. Instead, photon emission is the dominant contribution in the cooling curve, following the form seen in equation (5.13). Our simulation implements this by switching to

photon emission ODE, since the DM density is negligible. During this time the star can still be at an elevated temperature, e.g., above 1000 K. This is notable as old neutron stars, in the absence of external heating such as DM kinetic heating, are expected to be extremely cold (≤ 1000 K) [38]. This gives an observational probe for future neutron star surveys.

At each timestep, our simulation solves the ODE in equation 5.2. This process continues until the star exits the halo. When the star is between encounters, the same logic applies except the solver uses photon emission ODE in equation (5.13). With the temperatures calculated throughout the encounter history, we can now analyze the trends that result for each parameter set we considered.

7 Results

In this section we present and analyze the results of our simulations. We summarize three key outputs from our work;

I. The temperatures calculated by numerically solving the ODE in equation (5.2) over the unconstrained parameter space in Figure 13.

II. The amount of time that a neutron star spends at an elevated temperature, above 1000 K. We will denote this as f_{elev}, which represents the fraction of time the star spends above 1000K over its encounter history.

III. With the neutron star temperatures we can calculate the spectral flux densities corresponding to the subhalo masses and radii. This can impose further constraints to our subhalo parameter space to indicate which regions may yield observable neutron stars affected by kinetic heating.

7.1 Temperature Results

From the temperatures calculated through the star's encounter history, we determine the mean temperature it experiences. To do so, we must account for the time spent within halos being shorter than the time spent between encounters. We do this by taking the weighted average for the temperature, $\bar{T}_w$, with weights corresponding to the fraction of time spent inside f_{inner} and outside f_{outer} of the halos. The weights are then applied to the average temperature of the star when inside a halo $\bar{T}_{\text{inner}}$, and the average temperature when outside of halos $\bar{T}_{\text{outer}}$. Analytically, the weighted mean temperature (WMT) $\bar{T}_w$ is calculated as follows;

$$\bar{T}_w = \frac{(\bar{T}_{\text{inner}} \times t_{\text{inner}}) + (\bar{T}_{\text{outer}} \times t_{\text{outer}})}{t_{\text{inner}} + t_{\text{outer}}} = (\bar{T}_{\text{inner}} \times f_{\text{inner}}) + (\bar{T}_{\text{outer}} \times f_{\text{outer}}) \tag{7.1}$$

Figure 18 shows these values for corresponding subhalo parameters for NFW and uniform density subhalo encounters. Comparing the two, we see a difference in the temperature magnitude, with uniform density halos resulting in neutron stars ~ 600 K hotter than NFW halos. Comparing this to the smoothness parameter, we see that the elevated temperature contains parameters that indicate substructure presence. The lower third region is very diffuse in subhalo encounters, leading to average temperatures well below our threshold of 1000 K. Toward the upper third of the parameter space, we see the temperatures begin to approach a steady state around the initial 1500 K. Figure 20 shows this behavior, taking a uniform mass subhalo and increasing

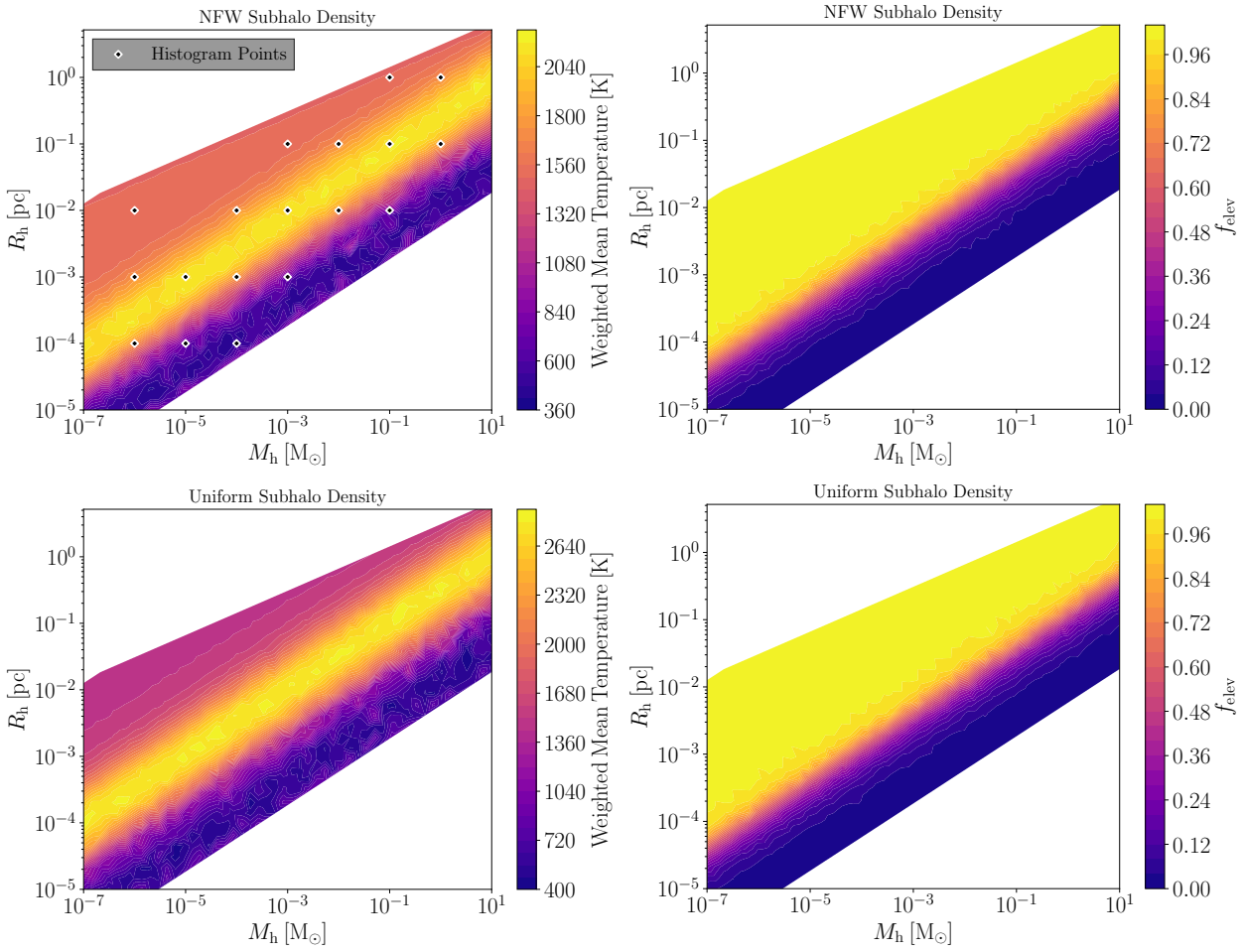

Figure 18: **Left Column:** Contour plots of the weighted mean temperature over the $(M_{\rm h}, R_{\rm h})$ parameter space, calculated using equation (7.1) for NFW (top) and uniform density (bottom) subhalos. We see the overall temperature trend remains similar between the two cases; a minimal heating region in the lower third region, a peak in temperature in the middle, and an approach to steady state in the upper third. **Right Column:** Contour plot of the fraction of time the neutron star spends at an elevated temperature $f_{\rm elev}$ through its encounter history with NFW (top) and uniform density (bottom) subhalos. From the lower region we again see the result of sparse encounter rates, with the star spending $< 40\%$ of their time above 1000 K. Moving further up in halo radii, toward the smooth DM distribution regime, $f_{\rm elev}$ increase, leading to a star spending a significant amount of time above 1000 K.

the radius until we see the temperature begin to fluctuate around T_0.

A benefit of our stochastic simulation is the ability to measure the variance in the mean temperature across the parameter space. To do this, we consider 18 parameter sets, indicated in Figure 18, and generate encounter histories to solve their cooling curves for 100 runs. We see in Figure 19 the temperature histograms for these simulations. The average temperature over all 100 runs is indicated by $\bar{T}_w$, which corresponds to the temperature readings shown in Figure 18. The standard deviation $\sigma_{\bar{T}}$ relative to the mean is calculated with

respect to $\bar{T}_w$, considering all temperatures for the $N = 100$ runs, denoted as T_j;

$$\mu_T = \sigma_{\bar{T}}/\bar{T}_w = \frac{1}{\bar{T}_w}\sqrt{\frac{\sum_{j=1}^{N}(T_j - \bar{T}_w)^2}{N}} \tag{7.2}$$

Comparing the trend in μ_T with the parameter space in Figure 18, we see the spread in temperatures gets tighter as the subhalo radius increases (or conversely, as the halo mass decreases). This can also be attributed to encounters becoming more frequent in the upper half of the unconstrained parameter space, leading to more consistent average temperatures as the DM distribution approaches steady state.

7.2 Time Spent Above 1000 K, f_{elev}

As the neutron star progresses through its encounter history, its temperature will change according to the ODE in equation (5.2). While passing through a halo, DM will increase its temperature due to kinetic heating. Once it exits the halo, it will no longer be heated by DM, but will be at a higher temperature than it was prior to its encounter. This will remain the case as photon emission cools the star between encounters. In the absence of heating sources, old neutron stars can be extremely cold, reaching temperatures below 1000 K. We use this as our threshold for designating a star as "kinetically heated". Most of the time the star spends at an elevated temperature is when it is cooling after an encounter. The time spent cooling from an initial temperature of T_i to a temperature of $T_f = 1000\,\text{K}$ can be calculated analytically using equation 5.15;

$$\Delta t_{\text{cool}} = \frac{1}{2\kappa}\left[\frac{1}{T_f^2} - \frac{1}{T_i^2}\right] \tag{7.3}$$

Over the course of its encounter history, we track the amount of time spent above 1000 K and compare it to the total time the simulation ran. This comparison gives us the fraction of time spent at an elevated temperature $f_{\text{elev}} \in [0,1]$;

$$f_{\text{elev}} = \frac{t_{\text{elev}}}{t_{\text{sim}}} \tag{7.4}$$

This was calculated for each parameter set that we ran in our simulation and plotted as a contour over the unconstrained space. This is shown in the right plot in Figure 18. Here we see the trend in f_{elev} follows closely with the DM distribution behavior;

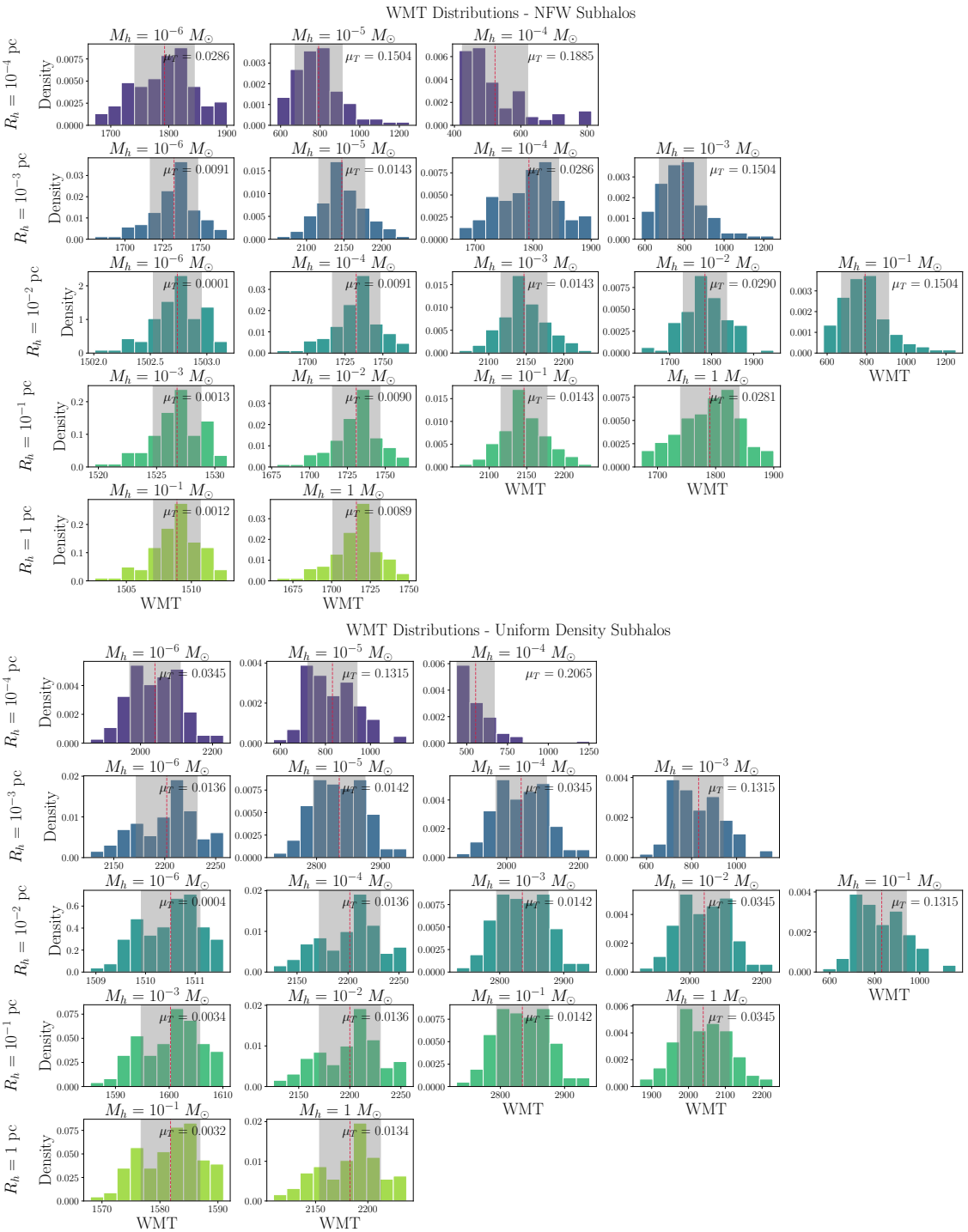

Figure 19: Temperature histograms for 18 subhalo parameter sets chosen from and indicated in Figure 18. We performed these runs for the cases of NFW (top) and uniform (bottom) DM halo densities. Each row is organized in terms of increasing halo mass M_h for the corresponding radius R_h. We see there is a larger spread in mean temperatures from uniform density halos compared to NFW halos, as indicated by the larger values of μ_T.

- **Infrequent Encounters:** The neutron star encounters very few subhalos over its encounter history.

  This results in very short moments of heating and therefore little time at temperatures above 1000 K.

- **Frequent Encounters:** The neutron star encounters many subhalos, constantly being affected by DM kinetic heating. The time between encounters τ_{enc} is much shorter due to the higher frequency of encounters, resulting in the majority of its time spent above 1000 K.

For very frequent encounters, Figure 18 shows values of $f_{elev} > 0.95$. This means that the subhalo number distribution is so high that there is very little time for photon emission to significantly lower the temperature of the star, resulting in a steady state neutron star. Despite the high frequency of encounters, the mean temperature observed in this regime is not substantially higher than it was initially, as seen in the $\bar{T}_w$ contour in Figure 18. We note that the encounter threshold of $N_{\text{Thresh}} = 500$ we imposed on our simulation results in shorter simulation times. This is due to how fast the threshold is reached in this region of the parameter space. We see in Figure 20 that despite a short simulation time, the temperature increases rapidly and begins to plateau very quickly.

On the other extreme, infrequent encounters result in minimal heating, with neutron stars spending $< 25\%$ of their time above 1000 K (Figure 18). This aligns with lower DM subhalo number densities.

Between these two cases, the central region of the contour plots show clumpy distributions that allow for a larger spread in mean temperatures compared to the high encounter frequency scenario. We see this well represented in the histograms shown in Figure 19 which were touched on in Section 7.1. Here we see a significant time ($> 50\%$) spent above 1000 K while providing indications of substructure.

7.3 Observation Prospects

Neutron star surveys have been proposed and would yield crucial information on neutron star formation, evolution, and on the presence of DM as we have explored in this work. Observational sensitivities have been the limiting factor for large survey. Since the neutron stars we are interested in are small (~ 10 km), old, and cold, they can be elusive targets for current telescopes.

It is therefore desirable for us to determine which ranges of subhalo parameters would yield neutron stars with temperatures favorable for observations. To do so, we consider the spectral flux density of a neutron star, described in Baryakhtar et al. [22];

$$f_\nu = \pi B\left(\nu, \bar{T}_w\right) \frac{4\pi \left(R_{NS}\gamma\right)^2}{4\pi d^2} \tag{7.5}$$

This is used to indicate the amount of energy being emitted by a blackbody, such as a neutron star, at a

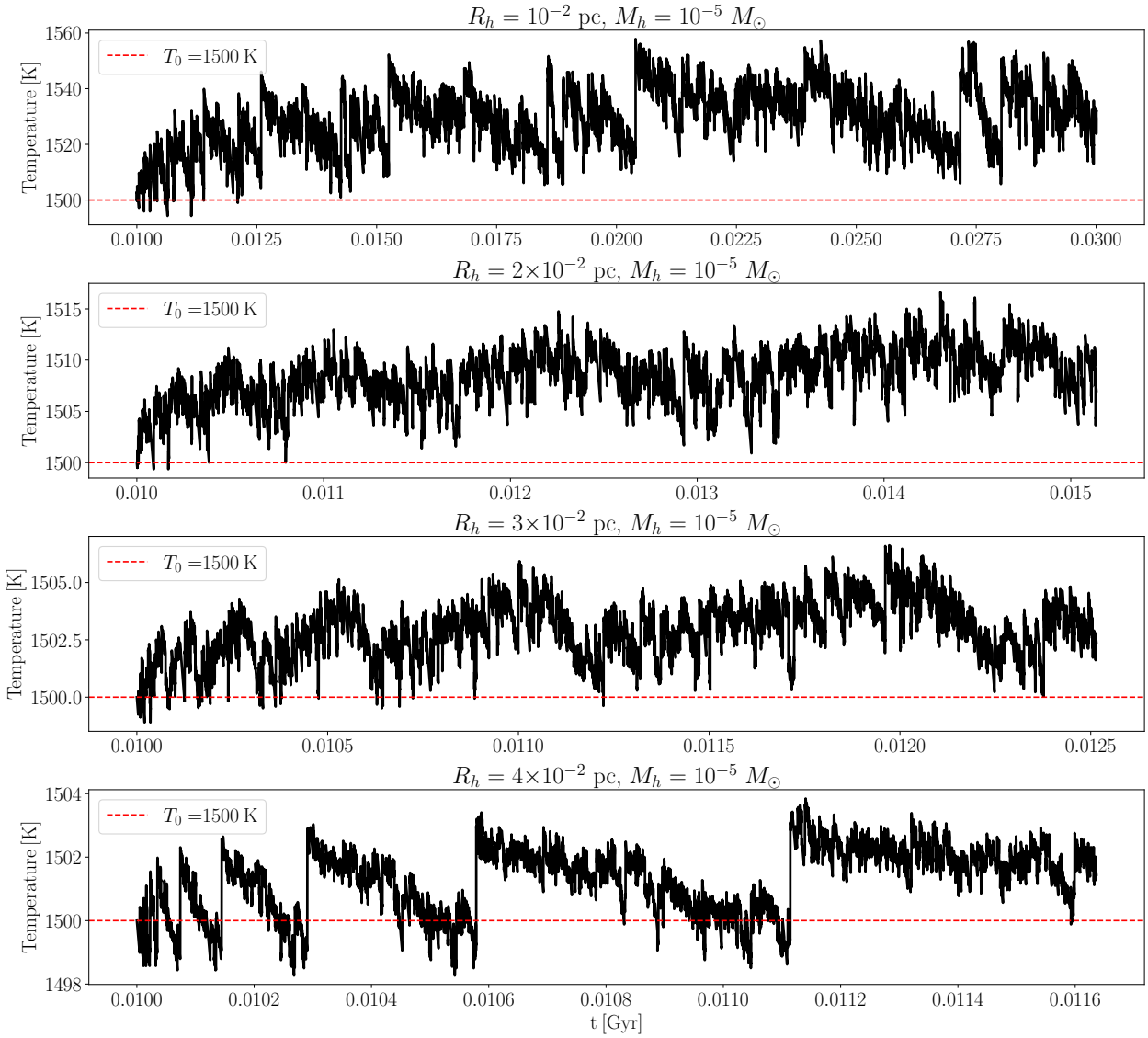

Figure 20: Cooling curves of the benchmark neutron star encountering subhalos of mass $M_h = 10^{-5}\,\mathrm{M}_\odot$ and radii $R_h = [1, 2, 3, 4] \times 10^{-2}\,\mathrm{pc}$. As the halo radius increases (i.e., more frequent encounters), the cooling curve converges closer to a steady state, fluctuating around the initial temperature of $T_0 = 1500\,\mathrm{K}$

given wavelength. This is especially important in astronomy for determining the sensitivities a telescope may have at different wavelength filters. Depending on exposure times, one could increase the sensitivity to observe fainter objects. The JWST NIRCam has a filter (F200W) that could be used to detect faint objects at 2 microns. For this filter, the exposure time with respect to the signal-to-noise ratio (SNR) scales as $\sqrt{t}$ [46]. For a SNR of 10, the exposure time is $\sim 10^4\,\mathrm{s}$ for a flux of $f_\nu^{\mathrm{JWST}} = 8\,\mathrm{nJy}$. Knowing how the SNR scales, the

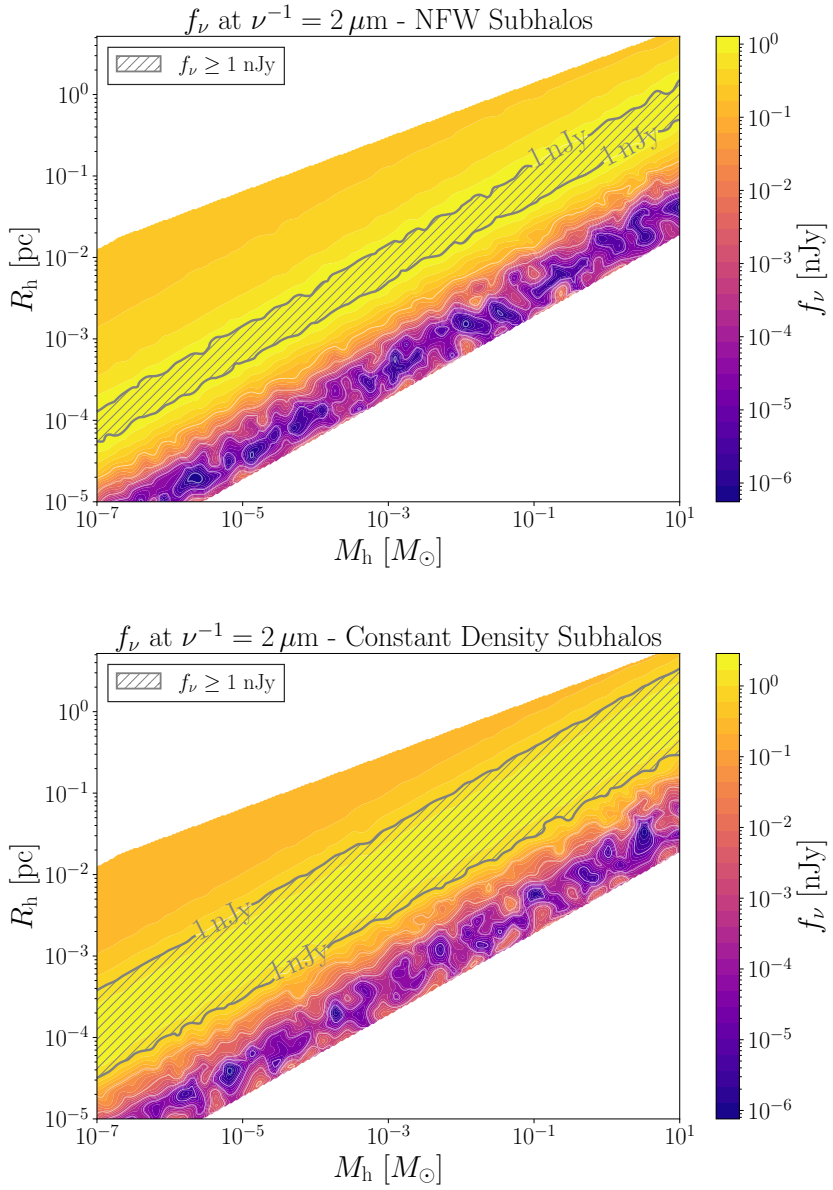

Figure 21: Contour plot of the spectral flux density f_ν at 2 microns based on the temperature contours from NFW (top) and uniform (bottom) density simulations shown in Figure 18. The hashed boundary defines fluxes ≥ 1 nJy, which can be potentially detected with long exposures using the NIRCam on JWST.

exposure time to observe a neutron star with a flux density of $f_\nu^{NS} = 1$ nJy follows as;

$$\frac{SNR_\mathrm{JWST}}{SNR_\mathrm{NS}} = \frac{f_\nu^\mathrm{JWST}}{f_\nu^\mathrm{NS}} \frac{\left(10^4\,\mathrm{s}\right)^{1/2}}{t_\mathrm{NS}^{1/2}}$$

$$t_\mathrm{NS} = \left(\frac{SNR_\mathrm{NS}}{SNR_\mathrm{JWST}} \frac{f_\nu^\mathrm{JWST}}{f_\nu^\mathrm{NS}} \left(10^4\,\mathrm{s}\right)^{1/2}\right)^2$$

$$= \left(\frac{8\,\mathrm{nJy}}{1\,\mathrm{nJy}} \left(10^4\,\mathrm{s}\right)^{1/2}\right)^2 = 640,000\,\mathrm{s} \sim 7.4\,\mathrm{days}$$

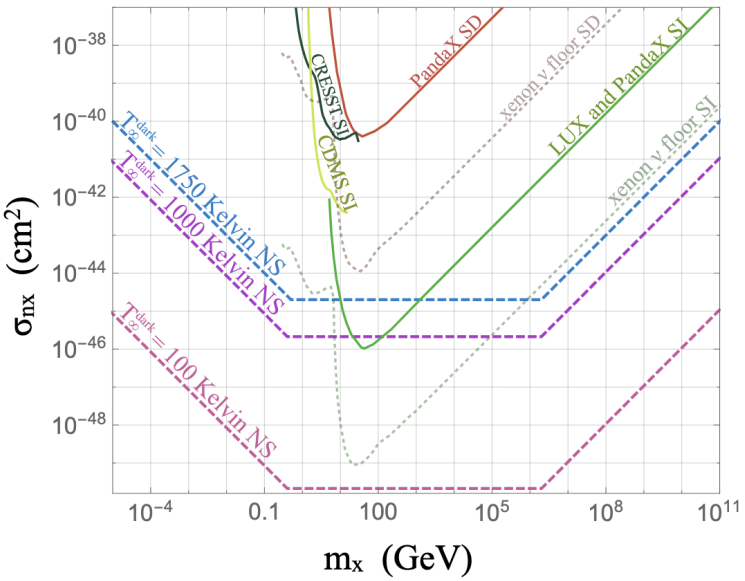

Figure 22: Expected constraints (dashed lines) on the DM-neutron scattering cross section if we observe a neutron star with temperatures of 1750 K, 1000 K, and 100 K. For a 100 K neutron star, this would indicate negligible heating from DM, ruling out a majority of scattering cross sections. Dotted and solid lines indicate pre-existing constraints from DD experiments.

To observe a neutron star at 1 nJy for an SNR of 10, one would require an exposure time of multiple days. This is a feasible sensitivity, and a significant amount of parameters in Figure 18, fall into this region. Figure 21 plots the flux densities for the corresponding temperatures over the parameter space. We see that $f_\nu \geq 1$ nJy contains many parameters in the region of elevated temperatures. We note that the uniform density halos appear to be much more promising in producing a larger observation region compared to NFW subhalos.

Observations of these neutron stars would yield cross section bounds similar to those imposed by LUX and PandaX as seen in Figure 22 from Baryakhtar et al. [22]. This would be crucial in further constraining DM interactions and mass regimes.

We note that these potential constraints (Figure 22) are under the assumption that DM has a smooth distribution. If we instead make the assumption that DM is clumpy/hierarchical, then the observation of a neutron star with a low temperature would not immediately rule out a large region of the parameter space. This is due to the rate of encounters a star could be experiencing, meaning an observed cold star could be within a cooling phase between subhalo encounters.

To test the results we have presented, large neutron star surveys would be required with sufficient sensitivities (≥ 1 nJy) to observe temperatures < 1000 K. If a large population of old neutron stars are surveyed, we can

determine how many are in an elevated state. If we were to observe a population of $N_{\rm obs}$ neutron stars, then the number of stars expected to be in an elevated state would be

$$N_{elev} = f_{\rm elev} \times N_{\rm obs} \tag{7.6}$$

The larger the population surveyed, the smaller the fractions we can probe. This can allow us to further constrain the subhalo parameter space (R_h, M_h).

8 Conclusion

From a cosmological standpoint, the presence of DM is vital in the evolution of our Universe, yet we have no idea what this invisible component truly is. DM affects the distribution and motions of visible matter, so we know that it interacts through gravity. The true question lies in how we can further investigate DM to truly understand it. Many particle theories have been proposed, such as CDM, that accurately describe how it behaves at large scales, but problems arise when attempting to apply the same models in describing small scale structure, such as the DM halos of galaxies. If DM can interact by means other than gravity, then this can help to describe its small scale behavior. Direct and indirect detection experiments continue their search for DM, using methods to detect potential scattering events or SM annihilation/decay products. Although we have yet to make such detections, these experiments have allowed us to constrain potential DM models. However, the continued lack of detection raises concerns about what we may be missing. The standard assumptions consider DM to have smooth distributions on small scales. In this case, one would assume that DM should have a non-negligible presence throughout the Milky Way. Without detections, this opens the door to explore changes to small scale DM distributions. Modifying early Universe cosmology can allow for DM to form substructures, e.g., subhalos, that would hold the majority of this invisible matter. The presence of these subhalos can provide a logical explanation for why we have not detected DM. For DD and ID experiments, it could very well be that the Earth, or target object, has yet to have an encounter. This is what we have presented in this thesis; a DM in the form of subhalos that interact with baryonic matter on time scales longer than our detection experiments have been online. These encounters can cause heating effects that can potentially be observed by current and next generation telescopes.

In our work, we studied a clumpy DM distribution for two cases; subhalos of uniform mass density, and halos that follow an NFW profile. For each case we examined how old, cold neutron stars encountering these subhalos can impact their cooling evolution. We probe a wide region in the subhalo mass and radius parameter space (M_h, R_h). We imposed initial constraints to these parameters by introducing a "clumpiness" parameter s (Section 4.4) to limit to parameters that would result in a clumpy distribution. This is paired with a constraint on the number of encounters per unit time of ~ 1 per 5 Gyr to allow for probing lower encounter rates. We also impose a constraint of $\Gamma_{\rm enc} = 10^7\,{\rm Gyr}^{-1}$ which accounts for the fact that no observations of DD have been made since they began collecting data. By considering the multiple encounter scenario, we introduce variability in how these stars are heated resulting in periods of elevated temperature. This is done

by sampling an encounter rate and impact parameter distribution for each subhalo encounter. From these simulations, we analyze the mean temperature over the simulation time, the relative standard deviation of 18 parameter sets, and the fraction of time the neutron star spends at an elevated temperature. We also use the mean temperature to calculate spectral flux densities to determine which subhalo parameters result in temperature increase potentially observable by JWST.

Our results show that by considering NFW and uniform density DM substructures, we obtain an observable increase in the average temperature of the star, particularly in the central region of the contour in Figure 18. We also find that the average temperature due to uniform density halos heating neutron stars can be $\sim 600\,\mathrm{K}$ higher than heating due to NFW halos. We also see that by introducing the sampling of the impact parameter b and the encounter rate Γ_{enc}, we observe a variance in the mean temperature. Since these quantities are dependent on the subhalo mass and radius, we see a trend in the deviation from T_w that correlates with the encounter rate in particular. As encounter rates become more frequent (smoother distributions), the tighter and more consistent the temperature distribution is.

Future neutron star surveys may provide important insights regarding our work and those performed previously in the area of DM heating in neutron stars. We acknowledge the necessity for telescopes such as TMT and ELT to build on the sensitivities of JWST. Neutron stars have long been a desirable laboratory for DM. As technology continues to advance, we must be ready to meet it with new ideas to push the boundaries of our understanding of DM and cosmology.

In this thesis we have provided the ground work for stochastic simulations of subhalo encounter with celestial bodies. We explored DM substructure by considering modifications to early Universe cosmology. Further studies can expand on our work by considering hierarchical density distributions; including a smooth component to studying effects of sustained heating during phases between halo encounters. Our results can also be built upon by extending the simulation parameter space to sub-Earth mass and radii subhalos, as seen in Bramante et al. [39].

Bibliography

[1] F. Zwicky, "Die Rotverschiebung von extragalaktischen Nebeln," *Helvetica Physica Acta*, vol. 6, pp. 110–127, Jan. 1933, aDS Bibcode: 1933AcHPh...6..110Z. [Online]. Available: https://ui.adsabs.harvard.edu/abs/1933AcHPh...6..110Z

[2] G. Efstathiou, "Challenges to the ΛCDM cosmology," *Phil. Trans. Roy. Soc. Lond. A*, vol. 383, no. 2290, p. 20240022, 2025.

[3] J. F. Navarro, C. S. Frenk, and S. D. M. White, "The Structure of cold dark matter halos," *Astrophys. J.*, vol. 462, pp. 563–575, 1996.

[4] W. J. G. de Blok, "The Core-Cusp Problem," *Adv. Astron.*, vol. 2010, p. 789293, 2010.

[5] N. Aghanim *et al.*, "Planck 2018 results. VI. Cosmological parameters," *Astron. Astrophys.*, vol. 641, p. A6, 2020, [Erratum: Astron.Astrophys. 652, C4 (2021)]. [Online]. Available: https://arxiv.org/abs/1807.06209

[6] V. C. Rubin, W. K. Ford, Jr., and N. Thonnard, "Extended rotation curves of high-luminosity spiral galaxies. IV. Systematic dynamical properties, Sa through Sc," *Astrophys. J. Lett.*, vol. 225, pp. L107–L111, 1978.

[7] V. C. Rubin, W. K. Ford, Jr., and N. Thonnard, "Rotational properties of 21 SC galaxies with a large range of luminosities and radii, from NGC 4605 (R=4kpc) to UGC 2885 (R=122kpc)." , vol. 238, pp. 471–487, Jun. 1980.

[8] D. Clowe, A. Gonzalez, and M. Markevitch, "Weak lensing mass reconstruction of the interacting cluster 1E0657-558: Direct evidence for the existence of dark matter," *Astrophys. J.*, vol. 604, pp. 596–603, 2004. [Online]. Available: https://arxiv.org/abs/astro-ph/0312273

[9] "Chandra x-ray observatory - images of 1e 0657-56," https://chandra.harvard.edu/photo/2006/1e0657/more.html.

[10] F. Zwicky, "On the Masses of Nebulae and of Clusters of Nebulae," , vol. 86, p. 217, Oct. 1937.

[11] G. O. Abell, "The Luminosity Function and Structure of the Coma Cluster," , vol. 213, pp. 327–344, Apr. 1977.

[12] A. A. Penzias and R. W. Wilson, "A Measurement of Excess Antenna Temperature at 4080 Mc/s." , vol. 142, pp. 419–421, Jul. 1965.

[13] B. Ryden, *Introduction to cosmology*, 2003.

[14] J. Billard, M. Boulay, S. Cebrián, L. Covi, G. Fiorillo, A. Green, J. Kopp, B. Majorovits, K. Palladino, F. Petricca, L. Roszkowski, and M. Schumann, "Direct Detection of Dark Matter – APPEC Committee Report," *Rep. Prog. Phys.*, vol. 85, no. 5, p. 056201, May 2022, arXiv:2104.07634 [hep-ex]. [Online]. Available: http://arxiv.org/abs/2104.07634

[15] B. R. Martin and G. Shaw, *Particle physics*, 2008.

[16] T. Lin, "TASI lectures on dark matter models and direct detection," Apr. 2019, arXiv:1904.07915 [hep-ph]. [Online]. Available: http://arxiv.org/abs/1904.07915

[17] E. Aprile *et al.*, "Observation and applications of single-electron charge signals in the XENON100 experiment," *J. Phys. G*, vol. 41, p. 035201, 2014.

[18] ——, "First Dark Matter Search with Nuclear Recoils from the XENONnT Experiment," *Phys. Rev. Lett.*, vol. 131, no. 4, p. 041003, 2023.

[19] M. Cirelli, A. Strumia, and J. Zupan, "Dark Matter," 6 2024.

[20] R. K. Leane and J. Tong, "Optimal celestial bodies for dark matter detection," *JCAP*, vol. 12, p. 031, 2024.

[21] M. L. Ahnen *et al.*, "Limits to Dark Matter Annihilation Cross-Section from a Combined Analysis of MAGIC and Fermi-LAT Observations of Dwarf Satellite Galaxies," *JCAP*, vol. 02, p. 039, 2016.

[22] M. Baryakhtar, J. Bramante, S. W. Li, T. Linden, and N. Raj, "Dark Kinetic Heating of Neutron Stars and An Infrared Window On WIMPs, SIMPs, and Pure Higgsinos," *Phys. Rev. Lett.*, vol. 119, no. 13, p. 131801, Sep. 2017, arXiv:1704.01577 [hep-ph]. [Online]. Available: http://arxiv.org/abs/1704.01577

[23] A. Joglekar, N. Raj, P. Tanedo, and H.-B. Yu, "Dark kinetic heating of neutron stars from contact interactions with relativistic targets," *Phys. Rev. D*, vol. 102, no. 12, p. 123002, 2020.

[24] D. Tucker-Smith and N. Weiner, "Inelastic dark matter," *Phys. Rev. D*, vol. 64, p. 043502, 2001.

[25] A. Heger, C. L. Fryer, S. E. Woosley, N. Langer, and D. H. Hartmann, "How Massive Single Stars End Their Life," , vol. 591, no. 1, pp. 288–300, Jul. 2003.

[26] N. Sartore, E. Ripamonti, A. Treves, and R. Turolla, "Galactic neutron stars: I. space and velocity distributions in the disk and in the halo," *Astronomy and Astrophysics*, vol. 510, p. A23, Feb. 2010. [Online]. Available: http://dx.doi.org/10.1051/0004-6361/200912222

[27] J. F. Acevedo, R. K. Leane, and A. J. Reilly, "Dark Kinetic Heating of Exoplanets and Brown Dwarfs," *J. High Energ. Phys.*, vol. 2025, no. 7, p. 79, Jul. 2025, arXiv:2405.02393 [hep-ph]. [Online]. Available: http://arxiv.org/abs/2405.02393

[28] D. A. Camargo, F. S. Queiroz, and R. Sturani, "Detecting Dark Matter with Neutron Star Spectroscopy," *J. Cosmol. Astropart. Phys.*, vol. 2019, no. 09, pp. 051–051, Sep. 2019, arXiv:1901.05474 [hep-ph]. [Online]. Available: http://arxiv.org/abs/1901.05474

[29] M. Pato, F. Iocco, and G. Bertone, "Dynamical constraints on the dark matter distribution in the Milky Way," *JCAP*, vol. 12, p. 001, 2015.

[30] S. Tulin and H.-B. Yu, "Dark Matter Self-interactions and Small Scale Structure," *Phys. Rept.*, vol. 730, pp. 1–57, 2018.

[31] V. Berezinsky, V. Dokuchaev, and Y. Eroshenko, "Remnants of dark matter clumps," *Phys. Rev. D*, vol. 77, p. 083519, 2008.

[32] S. Hofmann, D. J. Schwarz, and H. Stoecker, "Damping scales of neutralino cold dark matter," *Phys. Rev. D*, vol. 64, p. 083507, 2001.

[33] A. L. Erickcek and K. Sigurdson, "Reheating Effects in the Matter Power Spectrum and Implications for Substructure," *Phys. Rev. D*, vol. 84, p. 083503, 2011.

[34] M. O. Olea-Romacho, "Inflationary particle production and implications for WIMP substructure," *Phys. Rev. D*, vol. 113, no. 6, p. 063503, 2026.

[35] N. Blinov, M. J. Dolan, P. Draper, and J. Shelton, "Dark Matter Microhalos From Simplified Models," *Phys. Rev. D*, vol. 103, no. 10, p. 103514, 2021.

[36] Y.-Y. Mao, M. Williamson, and R. H. Wechsler, "The Dependence of Subhalo Abundance on Halo Concentration," *Astrophys. J.*, vol. 810, no. 1, p. 21, 2015.

[37] G. G. Raffelt, *Stars as laboratories for fundamental physics: The astrophysics of neutrinos, axions, and other weakly interacting particles*, 5 1996.

[38] D. G. Yakovlev, O. Y. Gnedin, M. E. Gusakov, A. D. Kaminker, K. P. Levenfish, and A. Y. Potekhin, "Neutron star cooling," *Nucl. Phys. A*, vol. 752, pp. 590–599, 2005.

[39] J. Bramante, B. J. Kavanagh, and N. Raj, "Scattering Searches for Dark Matter in Subhalos: Neutron Stars, Cosmic Rays, and Old Rocks," *Phys. Rev. Lett.*, vol. 128, no. 23, p. 231801, 2022.

[40] N. F. Bell, G. Busoni, S. Robles, and M. Virgato, "Thermalization and annihilation of dark matter in neutron stars," *JCAP*, vol. 04, p. 006, 2024.

[41] B. Bertoni, A. E. Nelson, and S. Reddy, "Dark Matter Thermalization in Neutron Stars," *Phys. Rev. D*, vol. 88, p. 123505, 2013.

[42] J. Bramante and N. Raj, "Dark matter in compact stars," *Phys. Rept.*, vol. 1052, pp. 1–48, 2024.

[43] D. G. Yakovlev, A. D. Kaminker, O. Y. Gnedin, and P. Haensel, "Neutrino emission from neutron stars," *Phys. Rept.*, vol. 354, p. 1, 2001.

[44] D. Page, U. Geppert, and F. Weber, "The Cooling of compact stars," *Nucl. Phys. A*, vol. 777, pp. 497–530, 2006.

[45] D. Page, J. M. Lattimer, M. Prakash, and A. W. Steiner, "Minimal cooling of neutron stars: A New paradigm," *Astrophys. J. Suppl.*, vol. 155, pp. 623–650, 2004.

[46] "Nircam iamaging sensitivity - jwst user documentation," https://jwst-docs.stsci.edu/jwst-near-infrared-camera/nircam-performance/nircam-sensitivity/nircam-imaging-sensitivity#gsc.tab=0.

Appendices

A Dark Matter Energy Depletion

This derivation for the energy depletion of a DM particle from a scattering interaction is based off the calculation done by Camargo et al. [28].

Here we provide a derivation of the energy loss of a DM particle scattering with a neutron within a neutron star. We define the 4-momentum of the DM particle and target neutron as follows;

$$P_\chi^\mu = \left(E_\chi, \overrightarrow{p}_\chi\right) \tag{A.1}$$

$$P_n^\mu = \left(E_n, \overrightarrow{p}_n\right) \tag{A.2}$$

The invariant norm of the four-momentum in the (1,-1,-1,-1) metric gives us an expression for the invariant mass of the particle;

$$P_{\mu,\chi}P_\chi^\mu = P_{\mu,\chi}^2 = m_\chi^2 c^2 = E_\chi^2/c^2 - \left|\overrightarrow{p}_\chi\right|^2 c^2 \underbrace{\rightarrow}_{c=1} E_\chi^2 = m_\chi^2 + \left|\overrightarrow{p}_\chi\right|^2 \tag{A.3}$$

$$P_{\mu,n}P_n^\mu = P_{\mu,n}^2 = m_n^2 c^2 = E_n^2/c^2 - \left|\overrightarrow{p}_n\right|^2 c^2 \underbrace{\rightarrow}_{c=1,\,|\overrightarrow{p}_n|=0} E_n = m_n \tag{A.4}$$

The four-momentum of the particles can then be written as follows;

$$P_\chi^\mu = \left(E_\chi, \overrightarrow{p}_\chi\right) \tag{A.5}$$

$$P_n^\mu = \left(E_n, \overrightarrow{0}\right) \tag{A.6}$$

The total four-momentum of the system is then,

$$P_{\text{total}}^\mu = \left(E_\chi + m_n, \overrightarrow{p}_\chi\right) \tag{A.7}$$

The invariant norm of the four-momentum for the system can then be calculated;

$$\begin{aligned} P_{\mu,\text{total}}P^{\mu}_{\text{total}} &= \left(E_{\chi}+m_n\right)^2 - |\overrightarrow{p}_n|^2 \\ &= E_{\chi}^2 + m_n^2 + 2E_{\chi}m_n - \left(E_{\chi}^2 - m_{\chi}^2\right) \\ &= m_{\chi}^2 + m_n^2 + 2E_{\chi}m_n \end{aligned} \tag{A.8}$$

Energy can be expressed in terms of the Lorentz boost γ as $E = \gamma m$. Since we know the invariant norm is $P_{\mu}P^{\mu} = m^2$, the Lorentz boost can be expressed as (with $c = 1$);

$$\gamma = \frac{E}{m} = \frac{E}{\sqrt{P_{\mu}P^{\mu}}} \tag{A.9}$$

We can also express the ratio of the particle velocity and c in terms of the momentum and energy as;

$$\beta = \frac{v}{c} = \frac{\gamma m v}{\gamma m c} = \frac{\gamma m v c}{\gamma m c^2} = \frac{pc}{E} \underbrace{\rightarrow}_{c=1} \frac{p}{E} \tag{A.10}$$

With the total energy of the system and equation A.8, the boost factor γ and β can be expressed as follows;

$$\gamma = \frac{E_{\text{total}}}{\sqrt{P_{\mu,\text{total}}P^{\mu}_{\text{total}}}} = \frac{E_{\text{total}}}{\sqrt{m_{\chi}^2 + m_n^2 + 2E_{\chi}m_n}} \tag{A.11}$$

$$\beta = \frac{p_{\text{total}}}{E_{\text{total}}} = \frac{\gamma m_{\chi} v_{\chi}}{E_{\chi} + m_n} \tag{A.12}$$

To work in the frame of the neutron star, we can transform the coordinates to the center of mass frame (CM). In the CM frame, the four-momentum of the target neutron is;

$$P^{\mu}_{\text{n}} = \left(E'_{\text{n}}, \overrightarrow{p}_{\text{n}}\right) \tag{A.13}$$

The momentum and energy in this frame are determined using the following Lorentz transformation;

$$E'_{\text{n}} = \gamma(E_n - \beta|\overrightarrow{p}_n|) \underbrace{\rightarrow}_{|\overrightarrow{p}_n|=0} \gamma E_n \tag{A.14}$$

$$\left|\overrightarrow{p}'_n\right| = \gamma(|\overrightarrow{p}_n| - \beta E_n) \underbrace{\rightarrow}_{|\overrightarrow{p}_n|=0} -\gamma\beta E_n \tag{A.15}$$

After scattering, the energy of the neutron can be expressed in terms of the scattering angle θ_s and its initial energy and momentum in the CM frame;

$$\begin{aligned} E'_{n,f} &= \gamma\left(E'_n + \beta p'_n\right) \\ &= \gamma(\gamma E_n + \beta\left(-\gamma\beta E_n\right)\cos\theta_s) \\ &= \gamma\left(\gamma E_n - \beta^2\gamma E_n \cos\theta_s\right) \\ &= \gamma^2 E_n\left(1-\beta^2\cos\theta_s\right) \end{aligned}$$

Subbing in the expressions for γ and β in equations (A.11) and (A.12), we get;

$$\begin{aligned} E_{n,f} &= \frac{\left(E_\chi + m_n\right)^2}{m_\chi^2 + m_n^2 + 2E_\chi m_n}\left[1 - \left(\frac{\gamma m_\chi v_\chi}{E_\chi + m_n}\right)^2 \cos\theta_s\right] E_n \\ &= \left(\frac{\left(E_\chi + m_n\right)^2}{m_\chi^2 + m_n^2 + 2E_\chi m_n} - \frac{\left(\gamma m_\chi v_\chi\right)^2 \cos\theta_s}{m_\chi^2 + m_n^2 + 2E_\chi m_n}\right) E_n \end{aligned}$$

Since $E_\chi = \gamma m_\chi v_\chi$, we can sub this into $E_{n,f}$;

$$\begin{aligned} E_{n,f} &= \frac{m_\chi^2 + \left(\gamma m_\chi v_\chi\right)^2 + m_n^2 + 2\gamma m_\chi m_n - \left(\gamma m_\chi v_\chi\right)^2 \cos\theta_s}{m_\chi^2 + m_n^2 + 2E_\chi m_n} E_n \\ &= \frac{m_\chi^2 + m_n^2 + 2\gamma m_\chi m_n + \left(\gamma m_\chi v_\chi\right)^2 (1 - \cos\theta_s)}{m_\chi^2 + m_n^2 + 2E_\chi m_n} E_n \\ &= \left(1 + \frac{\left(\gamma m_\chi v_\chi\right)^2 (1 - \cos\theta_s)}{m_\chi^2 + m_n^2 + 2E_\chi m_n}\right) E_n \end{aligned}$$

We can then rearrange by stating the change in energy of the DM particle as $\Delta E_\chi = E_{n,f} - E_n$, and subbing $E_n = m_n$ in the lab frame;

$$\Delta E_\chi = \frac{m_n m_\chi^2 \gamma^2 v_\chi^2}{m_\chi^2 + m_n^2 + 2\gamma m_\chi m_n}(1 - \cos\theta_s) \tag{A.16}$$

The velocity the DM particle has when it interacts with the neutron is equivalent to the escape velocity v_{esc} of the star $\left(v_\chi \simeq v_{\text{esc}}\right)$. This is due to the kinetic energy of χ being governed by the boost it receives when falling into the gravitational potential of the neutron star. Therefore, we can finally express the energy deposited by

the DM particle to be;

$$\boxed{\Delta E_\chi = \frac{m_n m_\chi^2 \gamma^2 v_{\rm esc}^2}{m_\chi^2 + m_n^2 + 2\gamma m_\chi m_n}\left(1 - \cos\theta_{\rm s}\right)} \tag{A.17}$$

Equation (A.17) is at a maximum when $1 - \cos\theta_{\rm s} = 1$.

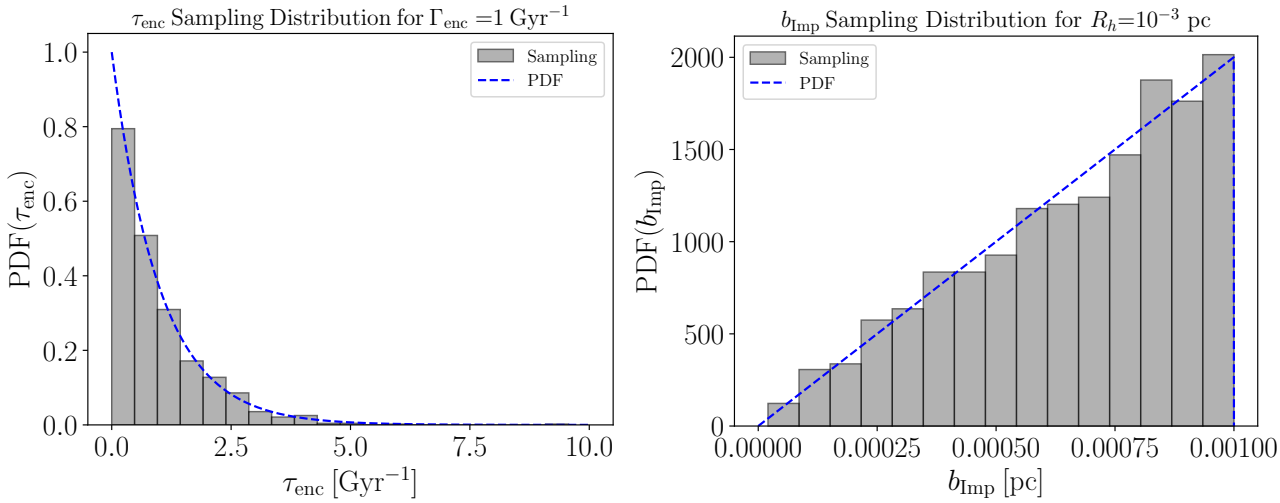

Figure 23: Sampling distribution for the time between encounters τ_{enc} (left) and the impact parameters b_{Imp} (right). The histograms in each plot are the results of the stochastic samples, which the dotted blue curves are the analytic forms of each distributions.

B Parameter Sampling Distributions

B.1 Time Between Encounters τ_{enc}

The analytic distribution function used to sample the time between subhalo encounters follows a decaying exponential,

$$PDF\left(\tau_{\text{enc}}\right) = \Gamma_{\text{enc}} \exp\left(-\Gamma_{\text{enc}} \tau_{\text{enc}}\right) \tag{B.1}$$

Where Γ_{enc} is defined in terms of (M_h, r_h) as,

$$\Gamma_{enc} = \frac{\rho_\chi}{M_h} \pi r_h^2 v_h \tag{B.2}$$

To confirm this distribution, a stochastic simulation was performed to gather the time between halo encounters. We consider the calculation of t_{imp}, i.e., the time in a subhalo trajectory that it impacts/begins its impact with a celestial body. A line between the initial state position of the ith subhalo and the position of starting its impact with, say, a star, follows the simple linear constant velocity equation of,

$$\mathbf{r}\left(t_{imp}\right) = \mathbf{r}\left(0\right) + v_h t_{imp} \tag{B.3}$$

Where v_h is the subhalo velocity. Therefore the time of impact is given to be,

$$t_{imp} = \frac{\mathbf{r}(t_{imp}) - \mathbf{r}(0)}{v_h} \tag{B.4}$$

Since this calculation in our simulation would go through each halo and calculate the time they impact, we must sort the final array from earliest to latest impact times. Once this is done, we calculate the difference between each element,

$$\tau_{\text{enc}} = |t_{imp,i+1} - t_{imp,i}| \tag{B.5}$$

With this new array of τ_{enc}, a histogram is plotted, as seen on the left of Figure 23 with the analytic distribution from equation B.1 shown as the overlaid dashed blue curve.

B.2 Impact Parameter b_{Imp}

For simplicity, we consider subhalos with spherical symmetry. This allows us to sample the impact parameters as a radial distribution for a circle. The function we then sample from has the form,

$$b_{\text{Imp}} = R_h \sqrt{\textbf{rand()}} \tag{B.6}$$

Where **rand()** is a uniform random sampling between 0 and 1. Here we have utilized inverse transform sampling from an initial PDF of,

$$PDF(b_{\text{Imp}}) = 2b_{\text{Imp}} \tag{B.7}$$

The result of the sampling is visualized in Figure 23 where we see the most likely values for b_{Imp} tend towards the outer regions of the halo.

C Neutron Star Cooling Curves - Example Derivations

This section outlines the derivations to the ODE in equation (5.2). There are three primary cases we consider; cooling curve from photon emission, uniform DM halo density, parabolic DM halo density.

C.1 Cooling Curve from Photon Emission

Neutron stars older than 10^5 yrs, in the absence of heating, experience cooling from photon emission;

$$\left(\frac{dT}{dt}\right)_{\gamma} = -\frac{\varepsilon_{\gamma}}{c_v} = -\kappa T^3 \tag{C.1}$$

Where κ combines the constants from the photon emissivity ε_{γ} and heat capacity c_v. For a neutron star of mass $M_{NS} = 1.5\,\mathrm{M}_{\odot}$ and radius $R_{NS} = 10\,\mathrm{km}$, the constant κ is calculated to be;

$$\kappa = \frac{4\pi\sigma_{SB}R_{NS}^2}{\beta V_{NS}}\left(1 - \frac{2GM_{NS}}{R_{NS}}\right) = 2.00748 \times 10^{-21}\ \mathrm{K}^{-2}\mathrm{s}^{-1} \tag{C.2}$$

Here we use $\beta = \frac{2\pi^2 k_B^2 m_n n_n}{3p_{F,n}^2}$ for the constants from c_v, as defined in equations (5.5) and (5.7). Integrating both sides of the ODE in equation (C.1);

$$\begin{aligned}
\int_{T_i}^{T_f} -\frac{1}{T^3}dT &= \int_{t_i}^{t_f} \kappa\, dt \\
\frac{1}{2T^2}\Big|_{T_i}^{T_f} &= \kappa t_f \\
\frac{1}{2}\left[\frac{1}{T_f^2} - \frac{1}{T_i^2}\right] &= \kappa t_f \\
\frac{1}{T_f^2} = 2\kappa t_f + \frac{1}{T_i^2} &= \frac{1}{T_f^2}\left[2\kappa T_i^2 t_f + 1\right]
\end{aligned}$$

This gives the following analytic solution for the temperature T_f after time $t_f - t_i$ for a neutron star cooled by photon emission;

$$\boxed{T_f = \frac{T_i}{\sqrt{2T_i^2\kappa\,(t_f - t_i) + 1}}} \tag{C.3}$$

Where $t_f - t_i = \Delta t_{\mathrm{cool}}$ is the time it takes to cool from an initial temperature T_i to a final temperature T_f.

C.2 Cooling Curve for a Uniform Density Halo

The simplest case for deriving the temperature of a neutron star as a function of time is to consider no cooling component and a uniform halo density profile. Since DM heating dominates over a short period of time while inside the halo, we can safely ignore cooling in this derivation. The ODE can then be simplified to just a single heating term;

$$\left(\frac{dT}{dt}\right)_\chi = \frac{\varepsilon_\chi}{c_v} = \frac{\Xi}{T}\rho_\chi \tag{C.4}$$

Similarly to the photon derivation in Appendix C.1, we use Ξ to absorb the constants from the DM emissivity ε_χ and the heat capacity c_v.

$$\Xi = \frac{1 - \frac{2GM_{NS}}{R_{NS}}}{\beta V_{NS}} \frac{(\gamma - 1)\,\pi b_{max}^2 v_\chi}{T} \tag{C.5}$$

Where v_χ is the DM velocity, and the impact parameter b_{max} follows from equation (3.10) as the maximum impact parameter for a DM particle to be captured gravitationally by the star. In this exercise we are considering a uniform spherical density for the halo, which has the form;

$$\rho_\chi = \frac{3M_h}{4\pi r_h^3}$$

Equation (C.4) can be solved analytically by integration;

$$\begin{aligned}
\int_{T_i}^{T_f} T\,dT &= \int_{t_i}^{t_f} \Xi \rho_\chi dt \\
\frac{1}{2}T^2\Big|_{T_i}^{T_f} &= \Xi\rho_\chi\,(t_f - t_i) \\
T_f^2 - T_i^2 &= 2\,\Xi\,(t_f - t_i)
\end{aligned}$$

$$\boxed{T_f = \sqrt{2\,\Xi\rho_\chi\,(t_f - t_i) + T_i^2}} \tag{C.6}$$

C.3 Cooling Curve for DM Halo with a Parabolic Density Profile

We begin by defining the following parabolic density profile as a function of halo radius, in terms of a scale density and radius (ρ_h, r_h):

$$\rho_\chi(r) = \rho_h\left(1 - \frac{r^2}{R_h^2}\right) \rightarrow \rho_h(t) = \rho_h\left(1 - \frac{\mathcal{R}(t)^2}{R_h^2}\right) \tag{C.7}$$

Here we re-parametrize the density profile in terms of time t through $\mathcal{R}(t)$ as described in equation (5.11). This allows us to integrate with respect to time to be consistent with our numerical solver. Similar to the uniform density case, we substitute the profile in equation (C.7) into the ODE in equation (5.2). The ODE with the substituted profile is similar to the uniform density case, but now with a time dependent density;

$$\frac{dT}{dt} = \frac{\Xi}{T}\rho_\chi(t)$$

where Ξ is taken from equation (C.5). We can now integrate both sides and solve for the final temperature T_f;

$$\begin{aligned}\int_{T_i}^{T_f} T\,dT &= \Xi\int_0^\tau \rho_\chi(t)\,dt \\ \frac{1}{2}\left(T_f^2 - T_i^2\right) &= \Xi\rho_h\int_0^\tau \underbrace{1}_{I_1} - \underbrace{\frac{\mathcal{R}(t)^2}{R_h^2}}_{I_2} dt\end{aligned}$$

We solve the integrals I_1 and I_2 as follows;

$$I_1 = \int_0^\tau t\,dt = \tau \tag{C.8}$$

$$\begin{aligned}I_2 &= \int_0^\tau \left(\frac{v_h^2}{R_h^2}(t-\alpha)^2 + \frac{b^2}{R_h^2}\right) dt \\ &= \frac{v_h^2}{3R_h^2}\left[(\tau-\alpha)^3 - \alpha^3\right] + \frac{b^2}{R_h}\tau\end{aligned} \tag{C.9}$$

Taking the results of I_1 and I_2, we find the following solution for the temperature T_f of the neutron star within a parabolic DM density halo;

$$\frac{1}{2}(T_f - T_i)^2 = \Xi\rho_h\left[\left(1 - \frac{b^2}{R_h^2}\right)\tau - \frac{v_h^2}{R_h^2}\left((\tau-\alpha)^3 + \alpha^3\right)\right]$$

$$\boxed{T_f = \sqrt{2\Xi\rho_h \left[\left(1 - \frac{b^2}{R_h^2}\right)\tau - \frac{v_h^2}{3R_h^2}\left((\tau-\alpha)^3 + \alpha^3\right)\right] + T_i^2}} \tag{C.10}$$